# CASE STUDY OF A JET CONTRAIL AT THE TROPOPAUSE: PROPERTIES, EVOLUTION AND RADIATIVE EFFECTS

by

Nathaniel Avery Mullins

A thesis submitted to the faculty of
The University of Utah
in partial fulfillment of the requirements for the degree of

Master of Science

Department of Meteorology

The University of Utah

August 2006

## ABSTRACT

On 13 July, 2002, the NASA WB-57F aircraft sampled its own condensation trail (contrail) near the tropopause between 15 and 16 km altitude during the Cirrus Regional Study of Tropical Anvils and Cirrus Layers-Florida Area Cirrus Experiment (CRYSTAL-FACE). In situ measurements of the contrail are used to estimate the net contrail radiative forcing ($CRF_{net}$).

The measurements show some fundamental differences between the WB-57F contrail and contrails measured at commercial flight altitudes between 8 and 13 km altitude. The WB-57F contrail was characterized by exceptionally high concentrations (on the order of 100 cm$^{-3}$) of small (primarily < 3 $\mu$m diameter) ice crystals that grew very slowly despite large ($\sim$40%) supersaturations with respect to ice. Values for the ice crystal effective radius $r_e$ averaged slightly less than 1 $\mu$m over the $\sim$20 minute sampling period; this value is considerably smaller than observed in previous studies. Mean ice water content $W$ was about 0.7 mg m$^{-3}$ with an estimated ice water path $WP$ of $\sim$0.1 g m$^{-2}$ and a mean optical depth of $\sim$0.2.

Radiative transfer modeling with sensitivity experiments shows that ice crystal size and water path $WP$ are the most significant influences on $CRF_{net}$ at the top of the atmosphere (TOA). For small ice water paths of $\sim$0.1 g m$^{-2}$, $r_e$ correlates negatively with $CRF_{net}$. For larger ice water paths (>1.0 g m$^{-2}$), the correlation between $r_e$ and CRF becomes positive. Differences in $CRF_{net}$ between the WB-57F contrail and lower altitude contrails are therefore primarily a function of the observed differences in $r_e$ and the amount of water flux from the aircraft, which depends on the size and type of aircraft and its fuel type and rate of combustion.

To all of my friends and family.

## TABLE OF CONTENTS

# List of Figures

# List of Tables

## ACKNOWLEDGMENTS

I would like to thank a number of individuals who have made this thesis possible and who have provided help and support through its composition. First I thank my advisor Dr. Tim Garrett for not only providing me the opportunity to become involved with the CRYSTAL-FACE mission, but for his patience, support, helpful advice, and attention to detail during the thesis editing process. I also thank my committee members Drs. Steve Krueger and Jay Mace, in addition to Dr. Kevin Perry, for their constructive feedback and willingness to help. I thank Department Chair Dr. Ed Zipser and other faculty and staff members for their help and encouragement as well. I thank Sally Benson for providing useful information regarding thesis requirements and deadlines. Finally, I thank Leslie Allaire and Kathy Roberts for keeping me informed of important deadlines and guidance regarding administrative tasks.

I would also like to thank the fellow scientists from CRYSTAL-FACE who graciously provided the data used in this study and aided in the interpretation of the data. Max Loewenstein and Hans-Jurg Jost provided CO data, and Stephen C. Wofsy provided $CO_2$ data. Tim Garrett provided

the light extinction data. Darrel Baumgardner provided measurements of the total particle concentration and size distribution from the Cloud and Aerosol Precipitation Spectrometer (CAPS). Robert Herman provided relative humidity data. T. Paul Bui provided measurements of temperature and pressure, turbulence and wind velocities using the Meteorological Measurement System (MMS). Karen Rosenlof provided the Global Positioning System (GPS) data that included latitude, longitude, and altitude of the aircraft, as well as aircraft velocity, attitude, pitch and roll.

In addition, I greatly appreciate the support, help and advice of many fellow graduate students. This includes Bradley Navarro, who assisted in analyzing data and compiling computer programs; Erik Crosman, who scanned Fig. 3.2; Merja Helena Schlueter, who assisted with graphics and word processing, and other students who provided assistance and support. Finally, I wish to express my appreciation for my friends and family, especially my parents, Stephen and Sara Mullins, who provided relentless love, encouragement and support through my course and research work as a graduate student.

# CHAPTER 1

# INTRODUCTION

Condensation trails from jet aircraft (contrails) have been a subject of interest to military weather forecasters and pilots since World War II (Coleman, 1996; Sassen and Hsueh, 1998). More recently, the radiative and climatic impacts of contrails have come under increased scrutiny because they are human induced, and they are increasing significantly in both frequency and coverage (Marquart et al., 2003).

Since contrails are a subset of upper tropospheric (UT) cloud cover, they are thought to alter the earth's radiative balance in a similar fashion to cirrus. Clouds near the surface of the earth tend to cause net cooling, because they reflect a relatively high percentage of solar radiation back to space and emit infrared (IR) radiation at temperatures similar to the earth's surface. The opposite is true for most cloud cover in the UT. Thin UT clouds such as cirrus and jet contrails tend to cause a small net warming effect (Hartmann et al., 1992): although they are relatively transparent to solar radiation, they decrease the loss of IR radiation at the top of the atmosphere (TOA) because they emit IR radiation at temperatures much

lower than the earth's surface.

The precise manner in which contrails alter solar and IR radiation fields depends on their temperature, single-scattering properties and coverage. Although recent field research has narrowed gaps in our understanding of contrails, there still exist many uncertainties. Measurements of the sizes of contrail ice crystals are uncertain by 20 to 30% (Baumgardner et al., 1992; Spinhirne et al., 1998), and ice crystal shape and orientation is not well resolved, resulting in corresponding uncertainties in radiative properties (Liou et al., 1998). Furthermore, while most researchers agree that contrails tend to cause instantaneous net cooling at the surface versus net warming at the TOA (Sassen, 1997; Wyser and Ström, 1998; Travis et al., 2004; ), direct measurement of contrail perturbations to clear sky radiative fluxes is nearly impossible above the lower stratosphere. Therefore, studies must rely on model calculations based on simplistic assumptions and highly uncertain input parameters; hence the magnitude and sign of climate perturbations from contrails remains unclear (Sassen, 1997).

## 1.1 Past observations of contrails

### 1.1.1 Retrieval methods

Until recently, remote sensing data have been the primary means of observing the properties and evolution of contrails (Duda et al., 1998). Traditionally, satellite data and ground based remote sensors have been

used to retrieve contrail effective radius and optical depth (e.g., Spinhirne et al., 1998; Meyer et al., 2002). The Subsonic Aircraft: Contrail and Cloud Effects Special Study (SUCCESS), a multiaircraft field campaign that took place over the central and western United States in April and May 1996, expanded understanding of chemical, microphysical and radiative properties of contrails through combined remote sensing and in situ measurements. Airborne platforms instruments included temperature, pressure and humidity sensors and spectrometers for measuring ice crystal size and density (Toon et al., 1998).

Good agreement was found between remotely sensed and in situ measurements. However, because mature contrails had properties similar to cirrus, distinguishing between the two based on satellite observations was difficult (Sassen and Hsueh, 1998; Spinhirne et al., 1998). While uncertainties in satellite and in situ measurements of particle size were similar (Baumgardner et al., 1992; Duda et al., 1998), in situ measurements of particle size tended to be smaller (Young et al., 1998).

### 1.1.2 Spatial properties and evolution

Contrail formation and evolution depends on the temperature, relative humidity, wind shear, static stability and baroclinicity of its environment (Chlond, 1998; Jensen et al., 1998; Kärcher, 2000; Duda et al., 2004). Vertical wind shear usually spreads the plume about an order of magni-

tude more rapidly in the horizontal than in the vertical (Chlond, 1998). In a supersaturated environment, contrails typically grow to about 0.5 to 1 km in depth and a few km in width within about 1 hour (Jensen et al, 1998; Spinhirne et al, 1998). Until precipitation becomes significant, the vertical spreading of the contrail depends primarily on aircraft wake dynamics (Lewellen, 2001) and is also influenced by atmospheric stability (Chlond, 1998).

A contrail plume may rise or fall due to buoyancy-driven updrafts and downdrafts, or radiative heating within the plume. In cases of substantial rising or sinking, the contrail plume may become obliquely oriented with respect to the horizontal plane (Jensen et al., 1998). Radiative heating rates within the plume can reach 10 K $day^{-1}$ and can lead to local updrafts that lift the contrail core several hundreds of meters (Jensen et al, 1998; Kärcher, 2000).

The evolution of the cross-sectional shape of the contrail is complex. Chlond (1998) suggested a nearly elliptical cross-section that stretches vertically over time due to gravitational settling of the largest ice crystals, with the center part of the plume stretching downward the farthest. Gierens (1996) and Ström and Gierens (2002) show a similar pattern of vertical settling in the center part of the contrail, in approximately a “U” shape. In both the horizontal and vertical planes, ice crystals sort with

time. Larger ice crystals have a higher mass to cross-sectional area ratio and thus higher fall velocities, and they also tend to sort towards the horizontal periphery of the contrail with smaller particles in the contrail core (Lawson et al., 1998; Spinhirne et al., 1998). This is probably due to turbulent processes within the contrail that force some ice crystals from the core to the periphery, which has higher supersaturations and is more conducive to ice crystal growth (Heymsfield et al., 1998; Lawson et al., 1998). The highest concentration of ice crystals generally remains in the center of the plume as it evolves. Consequently, this is where optical depths tend to be highest. The gradient in optical extinction tends to be positive vertically downwards and increases with time (Jensen et al., 1998; Ström and Gierens, 2002).

While the spatial evolution of the plume depends mainly on ambient conditions, the microphysical evolution is also influenced by aircraft fuel type (Gierens, 1996; Ström and Gierens, 2002). For example, Ström and Gierens (2002) showed that contrails forming from kerosene combustion tend to have higher ice crystal concentrations and optical depths than those that form from combustion of liquid hydrogen ($LH_2$). This is because kerosene has a higher molecular mass than $H_2$; hence its combustion yields a higher total water mass.

### 1.1.3 Microphysical observations

The microphysics of contrail ice crystals are influenced by meteorological conditions both within and without the plume. Particle size, size distribution, shape, orientation, spatial number density, and ice crystal growth rates are influenced by the temperature and humidity in the contrail (Sassen, 1997; Liou et al., 1998; Lewellen et al., 2001). These microphysical properties in turn determine the degree of scattering of solar radiation and absorption of terrestrial radiation by the contrail plume and the magnitude and sign of its radiative forcing (Liou, 2002).

Table 1.1 summarizes and provides metadata for several previous contrail studies, and Table 1.2 shows mean values of effective radius $r_e$, ice crystal number density $N$, ice water content $W$, optical depth $\tau$ and ice water path $WP$ from these studies. It is important to note that there is great temporal and spatial variability in $r_e$ in contrails. For example, in contrails at 10 km altitude, Duda et al. (1998) observed, based on satellite data, a mean $r_e$ in the 7 to 11 $\mu$m range, with higher values of 15 to 17 $\mu$m near the edges, for a contrail approximately 6 minutes of age. When the contrail had matured to 44 minutes old, $r_e$ had increased to 15 to 19 $\mu$m in the contrail core. In most cases, ice crystals grew by about an order of magnitude over a one-hour time scale following contrail formation (e.g., Liou et al., 1998; Sassen and Hsueh, 1998; Spinhirne et al., 1998; Meyer

et al., 2002). Also, a correlation between $T$ and $r_e$ can be seen in Fig. 1.1. This temperature-particle size relationship is mainly due to higher absolute humidities at lower altitudes that allow higher masses of water vapor to diffuse onto the ice crystals (Ström and Gierens, 2002) and may also be partially due to gravitational settling of larger particles. In addition, homogeneous nucleation favors smaller ice crystals at colder temperatures (Kärcher and Lohmann, 2002; Garrett et al., 2003).

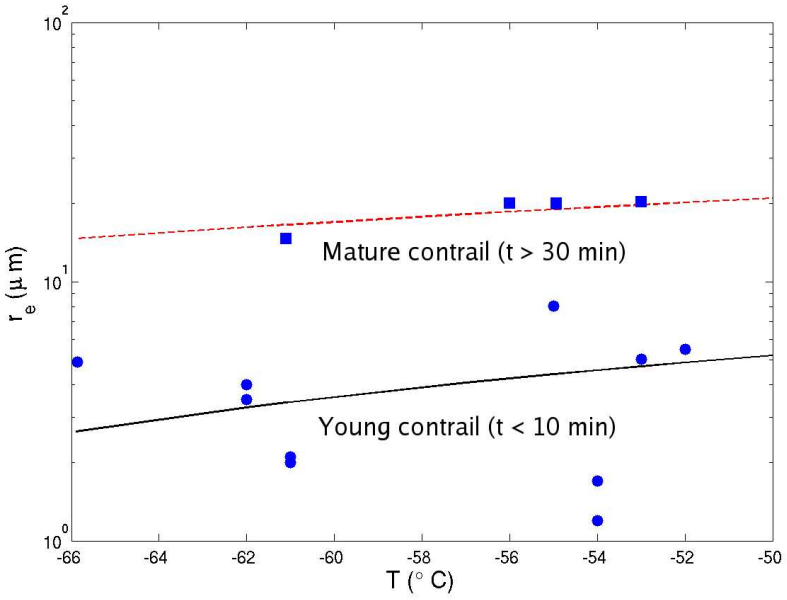


Figure 1.1: Values of $r_e$ plotted as a function of $T$ based on data from all authors listed in Tables 1.1 and 1.2 who give an effective radius at a temperature of -50° C or colder; data from model studies are excluded. The circles and squares represent data points from young and mature contrails, respectively.

Ice crystal shape affects the relative amount of radiation forward versus

Table 1.1: Details of previous contrail studies and the temperature at which the studies were conducted. The contrail age, source and measurement method are given. MASP, AWI, PCASP and FSSP refer to airborne instruments for particle size measurement.

| Author(s) | T (°C) | Age (min.) | Source | Method |
|---|---|---|---|---|
| Liou et al., 1998 | -65.9 | 1 | North Dakota Citation | replicator |
| Baumgardner et al., 1998 | -63 | | Boeing 757 | MASP |
| Khvorostyanov and Sassen, 1998 | -62 | | model sim | |
| Sassen, 1997 | -62 | 1 | various commercial | lidar |
| | | 60 | | |
| Liou et al., 1998 | -61.1 | 6 | Boeing 757 | |
| Goodman et al., 1998 | -61 | 1 | Boeing 757 | AWI, MASP |
| Jensen et al., 1998 (1) | -61 | 1 | model sim | |
| Sassen and Hsueh, 1998 | -57 | 6 | NASA DC-8 | lidar |
| | -57 | 60 | | |
| Shröder et al., 2000 | -57 | 2 | Boeing 737 | PCASP, FSSP |
| | | 10 | | |
| Gierens, 1996 | -56 | | model sim | |
| Toon et al., 1998 | -55 | | various | remote sensors |
| Lawson et al., 1998 | -55 | 40 | DC-8 | MASP |
| Shröder et al., 2000 | -54 | 1 | Airbus 310 | PCASP, FSSP |
| | | 3 | | |
| Chlond, 1998 | -53 | 8 | model sim | |
| | | 30 | | |
| Heymsfield et al., 1998 | -52 | | DC-8 | lidar, MASP |
| Jensen et al., 1998 (3) | -50 | 15 | model sim | |
| | | 30 | | |
| | | 60 | | |
| | | 75 | | |
| Spinhirne et al., 1998 | -50 | 6 | ER-2, DC-8 | lidar, satellite, in situ |
| | | 43 | | |
| Meyet et al., 2002 | -48 | | various commercial | |
| Minnis et al., 1998 | -41 | | DC-8, commercial | satellite |
| Ponater et al., 2002 | | | various commercial | satellite |
| Marquart et al., 2003 | | | various commercial | satellite |
| Duda et al., 1998 | | | unknown commercial | lidar, satellite |
| Gayet et al., 1996 | | | unknown commercial | lidar, FSSP-100 |

Table 1.2: Values of effective radius $r_e$, number density $N$, ice water content $W$, optical depth $\tau$ and ice water path $WP$ (calculated from the median values of $r_e$ and $\tau$) from the contrail studies listed in Table 1.1.

| Author(s) | $r_e$ ($\mu$m) | $N$ (cm$^{-3}$) | $W$ (mg m$^{-3}$) | $\tau$ | $WP$ (g m$^{-2}$) |
|---|---|---|---|---|---|
| Liou et al., 1998 | 4.9 | | | | |
| Baumgardner et al., 1998 | | 200 | 10-100 | | |
| Khvorostyanov and Sassen, 1998 | 3-5 | 1-10 | 1.6 | 0.15 | 0.37 |
| Sassen, 1997 | 2-5 | 10 | 2 | 0.07-0.42 | 1.53 |
| | 20-30 | | | | |
| Liou et al., 1998 | 13.3-15.9 | | | | |
| Goodman et al., 1998 | 1.9-2.3 | 6-13 | | | |
| Jensen et al., 1998 (1) | 1-3 | | | | |
| Sassen and Hsueh, 1998 | 1.5-5 | | | | |
| | 20-30 | | | | |
| Shröder et al., 2000 | 1.0 | 2150 | 3.9 | | |
| | 2.7 | 180 | 3.7 | | |
| Gierens, 1996 | 20 | | 2 | | |
| Toon et al., 1998 | 6-10 | | | 0.2-0.5 | 1.72 |
| Lawson et al., 1998 | 20 | | | | |
| Shröder et al., 2000 | 1.2 | 1100 | 3.2 | | |
| | 1.7 | 290 | 2.0 | | |
| Chlond, 1998 | 5 | 300 | 60 | | |
| | 20 | | | | |
| Heymsfield et al., 1998 | 1-10 | 10-100 | | | |
| Jensen et al., 1998 (3) | 5 | 3-20 | | 0.1-0.3 | 0.61 |
| | 10 | | | | |
| | 20 | | | | |
| | 25 | | | | |
| Spinhirne et al., 1998 | 7 | | 3.5 | 0.5 | 2.15 |
| | 20 | | | | |
| Meyet et al., 2002 | | | | 0.11 | |
| Minnis et al., 1998 | 6-13 | | | 0.3-0.4 | 1.84 |
| Ponater et al., 2002 | 12-15 | | 0.3-3.0 | 0.15 | 1.24 |
| Marquart et al., 2003 | 12-13 | | | 0.15 | 1.15 |
| Duda et al., 1998 | 5-15 | | | 0.1-0.5 | 1.84 |
| Gayet et al., 1996 | 20+ | | 10 | | |

backscattered (Liou, 2002). Relatively few contrail studies have focused on this aspect of crystal habit, and among those that have, observations have varied widely. Many authors (e.g., Spinhirne et al., 1998) assume that contrail ice crystals are spherical. Meyer et al. (2002) have suggested that ice crystals are quasi-spherical in young contrails, but as the contrail ages and the ice crystals grow, they become increasingly non-spherical. Alternatively, Liou et al. (1998) assumed 50% bullet rosettes, 30% hollow columns, and 20% hexagonal plates with no spheres, for effective radii on the order of 10 $\mu$m in contrails near 13 km altitude at a temperature of -62.9$^\circ$ C based on measurements from a replicator system aboard the NASA DC-8 aircraft. For small (2 $\mu$m) ice crystals formed at a similar temperature, Goodman et al. (1998) assumed 75% hexagonal plates, 20% hollow columns and 5% triangles also using replicator data. Bailey and Hallett (2004) suggested that larger ice crystals (150 to 300 $\mu$m) at temperatures of -70$^\circ$ C and supersaturations of 25% are primarily columns, needles, bullets and irregular shapes. Lawson et al. (1998) observed predominantly plates and columns with irregular and spheroidal shapes for ice crystals $< 20$ $\mu$m and mostly columns and bullet rosettes for ice crystals on the order of 100 $\mu$m, using a digital particle imager.

In general, the mean concentration of ice crystals decreases with contrail age (e.g., Jensen et al., 1998; Shröder et al., 2000; others). This rate of

decrease depends on several factors, including the relative humidity over ice within and without the plume and the rate at which new ice crystals are generated from entrainment of ambient air (Jensen et al., 1998). Concentrations peak immediately following contrail formation and, though highly variable from case to case, are usually on the order of 10 $cm^{-3}$. These values decrease to around 1 $cm^{-3}$ for contrails 45 to 60 minute old (Spinhirne et al., 1998).

Ice water content $W$ usually decreases from a few mg $m^{-3}$ to less than 1 mg $m^{-3}$ with age (Spinhirne et al., 1998; Twohy et al., 1998) but also varies greatly between cases. Gierens (1996) obtained values for $W$ of up to 10 mg $m^{-3}$ in young contrails from numerical simulations, while Khvorostyanov and Sassen (1998) observed a maximum $W$ of 1.6 mg $m^{-3}$ using ground-based lidar.

Mean optical depths $\tau$ in contrails typically peak in the 0.3 to 0.5 range and decrease with age. Meyer et al. (2002) calculated a relatively small optical depth of around 0.1, noting that there is a dependance of optical depth on wavelength of transmitted radiation and that this dependance itself depends on particle shape and size distribution. However, Duda et al. (1998) noted an increase in $\tau$ over time. Optical depths may exceed 1 for some young contrails and for contrails in warm, rising airmasses (Gayet et al., 1996; Meyer et al., 2002). A summary of values of $\tau$ from various

researchers is given in Table 1.2.

### 1.1.4 Radiative effects

Most researchers have suggested that contrails have a small positive net radiative forcing at the TOA, both regionally and globally. Over land and ocean, respectively, Meyer et al. (2002) calculated a mean TOA summer CRF of 8.9 W $m^{-2}$ and 9.9 W $m^{-2}$ and a TOA winter CRF of 4.4 W $m^{-2}$ and 8.4 W $m^{-2}$, assuming a whole-sky contrail coverage, a visible optical depth of 0.11, and land and ocean albedos of 0.2 and 0.05, respectively, at 50°N latitude. Ponater et al. (2002) estimated a global mean CRF of 0.4 mW $m^{-2}$ for an assumed sky coverage of 0.07%, or about a 0.6 W $m^{-2}$ forcing for a whole-sky coverage, an order of magnitude smaller than typical estimates. Marquart et al. (2003) estimated a global 2.3 W $m^{-2}$ whole-sky CRF in 1992 and projected a forcing of 6.1 W $m^{-2}$ for 2015 and 9.6 W $m^{-2}$ for 2050, assuming a doubling in optical depth over the next half-century. This forecast increase in optical depth is due to an expected quadrupling in jet fuel consumption combined with improved propulsion efficiency and a forecast increase in absolute humidities during this period. Sassen (1997) showed that substantial increases in annual jet fuel consumption during the mid 1960s were concurrent with a significant rise in annual mean surface temperature in the Salt Lake City, Utah region. Contrails are thought to decrease the surface diurnal temper-

ature range, through shortwave cooling during the daytime and longwave heating during the nighttime (Sassen, 1997; Travis et al., 2004).

Many researchers assume a whole-sky coverage to simplify radiative calculations, but the actual contrail CRF depends on the regional or global sky contrail coverage. Contrail frequency varies depending on atmospheric conditions, season, diurnal cycle, location, etc. (Minnis et al., 2003) and is not easily estimated. Meyer et al. (2002) estimated about 0.1% annual average contrail cover globally, but locally up to 3.0% annually averaged, based on extensive satellite observations of contrails over much of Europe and the northeastern Atlantic Ocean region, an area that historically has experienced the greatest frequency of contrail coverage. Ponater et al. (2002) estimated a mean global contrail coverage of 0.07% to 0.09%. Mean sky cover over the northeastern Atlantic and European region was estimated to be 0.5% by Chlond (1998) and Travis et al. (1997) with a peak coverage of about 2.0% over the transatlantic corridor (Chlond, 1998). Marquart et al. (2003) estimated a global contrail coverage of 0.07%, with the highest coverage of 0.88% over Western Europe, followed by the United States with 0.75%. By 2015, contrail coverage is expected to approximately double to 1.75% over Western Europe, 1.50% over the United States, and 0.15% globally.

## 1.2 CRYSTAL-FACE overview

The Cirrus Regional Study of Tropical Anvils and Cirrus Layers - Florida Area Cirrus Experiment (CRYSTAL-FACE) was conducted during late June and July of 2002. The primary scientific objective of the CRYSTAL-FACE mission was to enhance understanding of the characteristics of upper tropospheric cloud cover and its influence on the earth's climate using instrumentation not previously available (Jensen et al., 2004). Six aircraft, based at the Key West, FL Naval Air Station, were equipped with instruments that obtained in situ measurements of the microphysical, radiative and spatial properties and evolution of tropical cirrus over the South Florida peninsula and its surrounding waters. Flights were generally conducted every 2 days, depending on the meteorological conditions.

In addition to the airborne platforms, two ground sites were installed for CRYSTAL-FACE research, one on the east coast and the other on the west coast of the South Florida peninsula. These sites were equipped with ground-based lidars, radars, and radiometers for additional monitoring of cloud properties and meteorological conditions. Radiosondes were launched from PARSL, which was part of the western ground site. The GOES-8 and -10, NOAA AVHRR and MODIS satellites were also used. The NCAR S-band N-Pol radar was located at the western ground site, where operations were performed to identify and guide the aircraft into

clouds of research interest.

## 1.3 Study goals

Although CRYSTAL-FACE focused primarily on observing and measuring convective cirrus, contrails were also sampled. A contrail produced by NASA's WB-57F aircraft in the tropopause on 13 July provided a unique opportunity to study a persistent, spreading contrail that formed at a higher altitude and in different atmospheric conditions than previously observed. This contrail formed between 15 and 16 km altitude and at a mean temperature of -75° C in a highly supersaturated (with respect to ice) and stable atmosphere. The absence of ambient cloud cover allowed for measurements closely representative of the contrail itself, and the instrumentation aboard the WB-57F permitted easy in situ measurement of the cloud properties.

The primary objectives of this thesis are to:

- Identify the chemical, microphysical and single-scattering properties of the WB-57F contrail.
- Study the physical structure and evolution of the plume in space and time.
- Relate the contrail single-scattering properties to its perturbation of clear-sky fluxes.

- Compare the contrail's properties, evolution and radiative effects with those found in contrails studied previously at lower altitudes.

Chapter 2 will provide the theoretical background relevant to this case study as a context for interpreting the results both quantitatively and qualitatively. Chapter 3 will discuss the WB-57F instruments that collected data for this study and their functions and limitations. Chapter 4 will present the data and observations from sampling of the WB-57F contrail. Chapter 5 will discuss the radiative effects of contrails with microphysical and single-scattering properties from the 13 July case. Finally, Chapter 6 will summarize the key findings from this study, compare the results with those from other contrail studies, and suggest possible areas of future work.

# CHAPTER 2

# THEORETICAL BACKGROUND

## 2.1 Radiative properties

This section describes how ice crystal single scattering parameters relate to contrail radiative forcing.

The attenuation or 'extinction' of a direct beam of radiation by atmospheric particles is proportional to the combined scattering and absorption cross-sections ($\sigma_s$ and $\sigma_a$):

$$\sigma_{ext} = \sigma_s + \sigma_a, \tag{2.1}$$

where cross-sections are related to the projected area $A$ normal to the beam through the efficiencies $Q_s$ and $Q_a$:

$$\sigma_s = Q_s A \tag{2.2}$$

and

$$\sigma_a = Q_a A. \tag{2.3}$$

For transparent cloud particles large with respect to the wavelength $Q_a = 0$ and $Q_s \approx 2$. The single scattering albedo $\omega_0$ is defined as:

$$\omega_0 = \frac{\sigma_s}{\sigma_{ext}} \approx \frac{Q_s}{Q_s + Q_a}, \tag{2.4}$$

which represents the probability that a photon is scattered by a particle; $\omega_0 \approx 1$ if $Q_a = 0$ and $Q_s \approx 2$. The extinction coefficient $\beta_{ext}$ and optical depth $\tau$ are related to $\sigma_{ext}$ by:

$$\beta_{ext} = \int_0^\infty \sigma_{ext} n(A) dA, \tag{2.5}$$

where $n(A)$ is the concentration of particles with projected area $A$, and

$$\tau = \int_{z_b}^{z_t} \beta_{ext}(z) dz, \tag{2.6}$$

where $z_b$ and $z_t$ are the base and top of the cloud, respectively. Note that $\beta_{ext}$ has units of inverse length, while $Q_s$, $Q_a$, $\omega_0$ and $\tau$ are dimensionless.

The angular distribution of radiation scattered by atmospheric particles is expressed in terms of a phase function $P(\mu)$, where $\mu$ is the cosine of the scattering angle. For studies of climate, only the first moment of $P(\mu)$ or the asymmetry factor $g$ is considered (Liou 2002), where:

$$g = \frac{1}{2} \int_{-1}^{1} P(\mu) \mu d\mu. \tag{2.7}$$

For perfectly symmetric (e.g., Rayleigh) scattering $g = 0$. For complete forward scattering $g = 1$ and for complete backscattering $g = -1$.

The magnitude and sign of $g$ depends on the size, shape and orientation of particles, and the wavelength of incident radiation (Lawson et al., 1998). Mie theory predicts predominantly forward scattering by particles much larger than the incident wavelength. For 10 $\mu$m diameter ice crystals composed of 50% bullet rosettes and aggregates, 30% hollow columns, and 20% plates, calculated values for $g$ are around 0.8 for radiation at visible wavelengths (Liou, 2002). By comparison, measured values of $g$ are $\sim$ 0.74 in Arctic cirrus (Garrett et al., 2001). The exact relationship between $g$ and crystal habit remains uncertain due to difficulties in relating scattering to ice crystal shape.

The net radiative forcing at the top of the atmosphere (TOA) by a contrail $CRF_{net}$ is defined as the sum of the net solar forcing $CRF_{netsw}$ and the net infrared forcing $CRF_{netlw}$:

$$CRF_{net} = CRF_{netsw} + CRF_{netlw}, \tag{2.8}$$

where

$$CRF_{netsw} = SW_{netobs} - SW_{netclear} \tag{2.9}$$

and

$$CRF_{netlw} = LW_{netobs} - LW_{netclear} \tag{2.10}$$

where, $SW_{netobs}$ and $SW_{netclear}$ are the observed and the clear-sky net solar fluxes, respectively and, $LW_{netobs}$ and $LW_{netclear}$ are the observed and the clear-sky net infrared fluxes, respectively (Key, 2001).

Larger values of $\tau$ correspond to larger absolute values of $CRF_{netsw}$ and $CRF_{netlw}$ (Hartmann, 1994; Liou, 2002). At small optical depths (e.g., $\tau = 0.1$) $CRF_{net}$ is usually positive in contrails because $|CRF_{netlw}| > |CRF_{netsw}|$. For small values of $\tau$, the values of $CRF_{net}$ and $\tau$ are positively correlated, because $|CRF_{netlw}|$ increases more rapidly than $|CRF_{netsw}|$. The value of $CRF_{net}$ is maximized at a certain "critical" value of $\tau$, which if surpassed, $|CRF_{netsw}|$ increases more rapidly than $|CRF_{netlw}|$. The sign of $CRF_{net}$ changes when $|CRF_{netsw}| > |CRF_{netlw}|$ (e.g., Sassen, 1997; Garrett et al., 2003).

For radiative flux calculations, usually only $\omega_0$, $\tau$ and $g$ are considered. There exist many algorithms for determining net shortwave and longwave radiative fluxes and $CRF_{net}$ based on these parameters. Here, the radiative transfer model Streamer (Key, 2001) is used. Further description of this model is provided in Section 5.1.

## 2.2 Contrail formation and microphysics

### 2.2.1 Contrail formation

Contrails form due to enhanced relative humidities from the mixing of warm, moist exhaust gases with ambient air. Water vapor within the plume deposits or 'freezes' on aerosols that are either preexisting or emitted by the aircraft following fuel combustion. Fig. 2.1 shows the thermodynamic relation for the formation of contrails with regards to temperature and water vapor partial pressure inside the plume. Aircraft exhaust emitted at point A (with water vapor partial pressure and temperature well outside the graph) will cool and dry as it mixes with the ambient air. The mixture will stop cooling and drying when its temperature and water vapor partial pressure are in equilibrium with the ambient air, represented by point B (which is reached asymptotically for a constant atmospheric state). The point at which the line formed between points A and B initially crosses the liquid water saturation curve represents initial contrail formation. If this line crosses the ice saturation curve, the contrail ice crystals will sublimate, in the absence of secondary radiative or dynamical effects (Kärcher, 2000). Should the air parcels remain saturated with respect to ice for an extended period of time, a persistent contrail may develop (Schröder, 2000).

Fig. 2.2 shows the threshold ambient temperature $T$ and saturation ratio $S_a$ for contrail formation in both tropical and mid-latitude atmospheres.

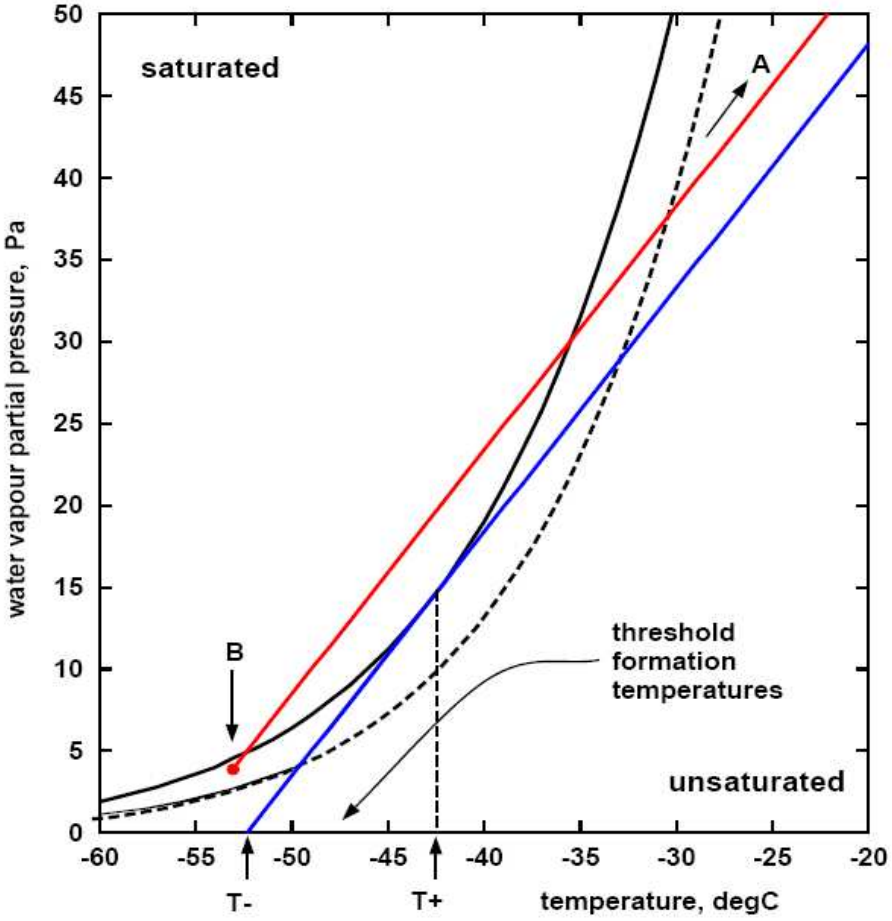


Figure 2.1: Diagram showing $H_20$ saturation vapor pressures with respect to liquid water (solid curve) and ice (dashed curve). Line A-B (shown in red) represents an air parcel inside a contrail plume mixing isobarically with the cooler and drier ambient air as the contrail ages. The tangent line (blue) paralleling the red line is used to derive the threshold temperature for contrail formation. $T^-$ is the threshold temperature for formation in dry air, and $T^+$ is the threshold temperature for formation in saturated air (from Kärcher 2000).

At any flight altitude below the altitude of intersection of the mid-latitude and tropical profiles in Fig. 2.2 ($\sim$200 mb), contrails require a lower ambient humidity to form at mid-latitudes than in the tropics. However, at flight levels above this altitude, the opposite is true because the tropical tropopause is colder, and contrails will always form for any value of $S_a$.

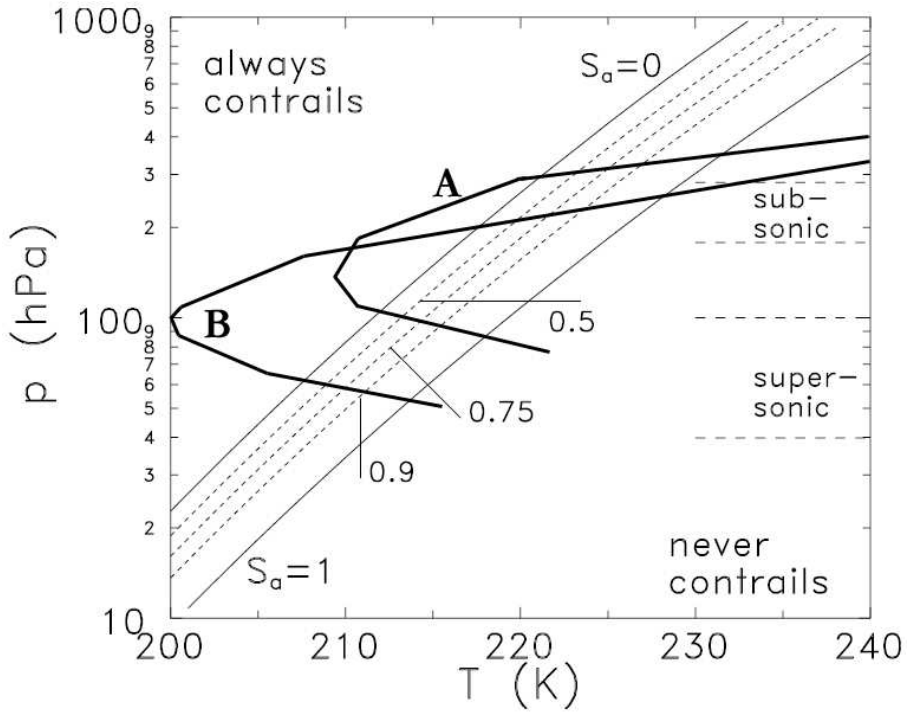


Figure 2.2: Diagonal curves representing pressure altitudes of contrail formation at a given ambient temperature, parameterised by the ambient $H_2O$ saturation ratio (relative humidity divided by 100%) required for contrail formation. Standard (mid-latitude) and tropical atmospheric profiles obtained from Hartmann (1994) are superimposed on the plot and labeled "A" and "B", respectively (adapted from Kärcher 2000).

### 2.2.2 Contrail microphysics

A characteristic radiative length scale often used to relate cloud mass to its optical properties is its "effective radius" $r_e$. Assuming particles are spherical, $r_e$ can be defined as the third moment (total volume of cloud matter) divided by the second moment (total cross-sectional area) of the size distribution (Stephens et al., 1978):

$$r_e = \frac{\int_0^\infty \pi n(r) r^3 dr}{\int_0^\infty \pi n(r) r^2 dr}. \tag{2.11}$$

An equivalent, but more general definition of $r_e$ suitable for all shapes is proportional to the ratio of the water content $W$ and the optical extinction coefficient $\beta_{ext}$ . If the extinction efficiency $Q_{ext}$ is 2, as is the case for particles that are large with respect to the wavelength of incident radiation, then

$$r_e = \frac{3W}{2\rho\beta_{ext}}, \tag{2.12}$$

where $\rho$ is the bulk density of ice or liquid water.

Alternatively,

$$r_e = \frac{3WP}{2\rho\tau}, \tag{2.13}$$

where

$$WP = \int_{z_b}^{z_t} W(z)dz. \tag{2.14}$$

Thus a contrail with a high total scattering cross-sectional area has a smaller $r_e$ for equivalent mass and therefore scatters incident radiation more effectively.

Ice crystal size distributions change constantly, due to variability in temperature, humidity, and wind fields. Ice crystals grow by either water vapor diffusion or aggregation. In the case of contrails, ice crystal growth occurs primarily due to deposition of water vapor in supersaturated conditions. Aggregational growth is insignificant due to the low relative fall velocities of the ice crystals and the low probability of collisions that stick at very low temperatures (Gierens et al, 1996).

The condensational (depositional in the case of ice) growth rate equation for a hydrometeor within a supersaturated environment is (Rogers and Yau, 1989):

$$r(t) = \sqrt{\left((r_0)^2 + 2\xi t\right)}, \tag{2.15}$$

where $r$ is the particle radius, $r_0$ is the initial radius, $t$ time, and

$$\xi = r\frac{dr}{dt} \equiv \frac{(S-1)}{(F_k + F_d)}, \tag{2.16}$$

where $S = e/e_s(T)$ is the ambient saturation ratio. For particle sizes of at

least several tens of $\mu$m, a radiative heating term should also be included in Eq. 2.16. However, for the low radiative heating rates found in contrails, this term is negligible (Chlond, 1998). $F_k$ and $F_d$ are the thermodynamic heat conduction and vapor diffusion factors, respectively. $F_d$ is defined as

$$F_d = \frac{\rho_i R_v T}{D_{vm} e_s(T)}. \tag{2.17}$$

$R_v$ is the specific gas constant for water vapor, $T$ is the temperature in degrees Kelvin, $\rho_i$ is the density of ice, $e_s$ is the ambient saturation vapor pressure, and $D_{vm}$ is the modified diffusivity parameter of water vapor in air (Pruppacher and Klett, 1989). For high altitudes and cold temperatures, $F_d >> F_k$.

The modified diffusivity parameter $D_{vm}$ is expressed as follows:

$$D_{vm} = \frac{D_v}{\left[\frac{r}{r+C\lambda} + \frac{D_v}{r\alpha_c}\sqrt{\frac{2\pi M_w}{R_d T}}\right]}, \tag{2.18}$$

where

$$\lambda = \lambda_0 (\frac{P_0}{P})(\frac{T}{T_0})^{1.94}, \tag{2.19}$$

where $\lambda_0 = 0.064$ $\mu$m is the mean free path of air at STP, $C = 0.7$, and $r$ is the particle radius in $\mu$m. $D_v$ is the diffusivity of water vapor in air, $R_d$ is the specific gas constant of dry air, $M_w$ is the molecular mass of water, and $\alpha_c$ is the deposition coefficient, which is not well constrained for ice.

The modified diffusivity is used here to account for kinetic limitations to the growth of particles smaller than 1 $\mu$m radius (Pruppacher and Klett, 1997).

# CHAPTER 3

# MEASUREMENTS

The WB-57F (Fig. 3.1) was equipped to measure in situ upper tropospheric chemistry, cloud and meteorological properties. During the flight on 13 July, 2002, the WB-57F measured these properties within its own contrail at the tropopause between 15 and 16 km altitude. Mean air speeds were about 190 m $s^{-1}$ during contrail sampling. The WB-57F flew along the length of the contrail over a period of $\sim$20 minutes between 1932 and 1952 UTC.

Table 3.1 summarizes the instruments aboard the WB-57F. Details of these instruments are presented in this chapter.

## 3.1 Chemistry

The Ames Research Center Argus instrument took in situ measurements of carbon monoxide (CO) with a data acquisition rate of 0.5 Hz. The Argus is an absorption spectrometer that operates in rapid-scan, simple harmonic mode and uses frequency modulated tunable lead-salt diode lasers to emit infrared (IR) radiation through a Herriott cell. The preci-


Figure 3.1: The NASA WB-57F used during the CRYSTAL-FACE mission.

Table 3.1: Instruments aboard the NASA WB-57F

| Variable(s) | Instrument | Manufacturer |
|---|---|---|
| Aircraft velocity and position | Global positioning system | NASA WB-57F Navigation System |
| Temperature, pressure and wind fields | Meteorological Measurement System | NASA Ames Research Center |
| Relative humidity | Laser hygrometer | Jet Propulsion Laboratory |
| Extinction coefficient | Cloud integrating nephelometer | Gerber Scientific, Inc. |
| Aerosol size distribution | Cloud aerosol precipitation spectrometer | Droplet Measurement Techniques |
| Carbon monoxide (CO) | Argus instrument | NASA Ames Research Center |
| Carbon dioxide ($CO_2$) | High-altitude fast-response $CO_2$ analyzer | NASA Goddard Space Flight Center |

sion of the instrument depends on atmospheric pressure and is 1.1 ppbv at 268 mb and 2.2 ppbv at 77 mb. Assuming this increase in precision with altitude is linear, the precision at the altitude of the 13 July contrail ($\sim$125 mb), is $\sim$2.0 ppbv. The accuracy of the Argus instrument is 3% (CRYSTAL-FACE website).

The instrument used to measure Carbon Dioxide ($CO_2$) was the NASA Goodard Space Flight Center's High-Altitude Fast-Response $CO_2$ Analyzer. In situ $CO_2$ concentrations were measured using a light source, gas cells, and a solid-state detector from a modified nondispersive infrared $CO_2$ analyzer. The $CO_2$ mixing ratio of air flowing through the sample gas cell is determined by measuring absorption of IR radiation (4.26 $\mu$m) relative to a reference gas of known concentration. Both the accuracy and precision of the instrument are 0.1 ppm at a measurement frequency of 0.5 Hz (CRYSTAL-FACE website).

## 3.2 Microphysical and bulk properties

Size distributions of atmospheric particles were measured using the Droplet Measurement Technologies (DMT) Cloud Aerosol Precipitation Spectrometer (CAPS). The CAPS combines the Cloud Aerosol Spectrometer (CAS), which sizes particles between 0.5 and 50 $\mu$m diameter, with the Cloud Imaging Probe (CIP), which images particles larger than 25 $\mu$m diameter (Baumgardner et al., 1992). Because virtually all ice crystals

within the contrail studied were less than 10 $\mu$m diameter, only CAS measurements are described here.

The measurement principle of the CAS is similar to that of the Forward Scattering Spectrometer Probes (FSSP) Models 100ER and 300, widely used in the past by researchers measuring clouds. The FSSP infers particle size from measurements of the intensity of radiation scattered between 4° and 12° by hydrometeors based on Mie theory calculations (see Fig. 3.2).

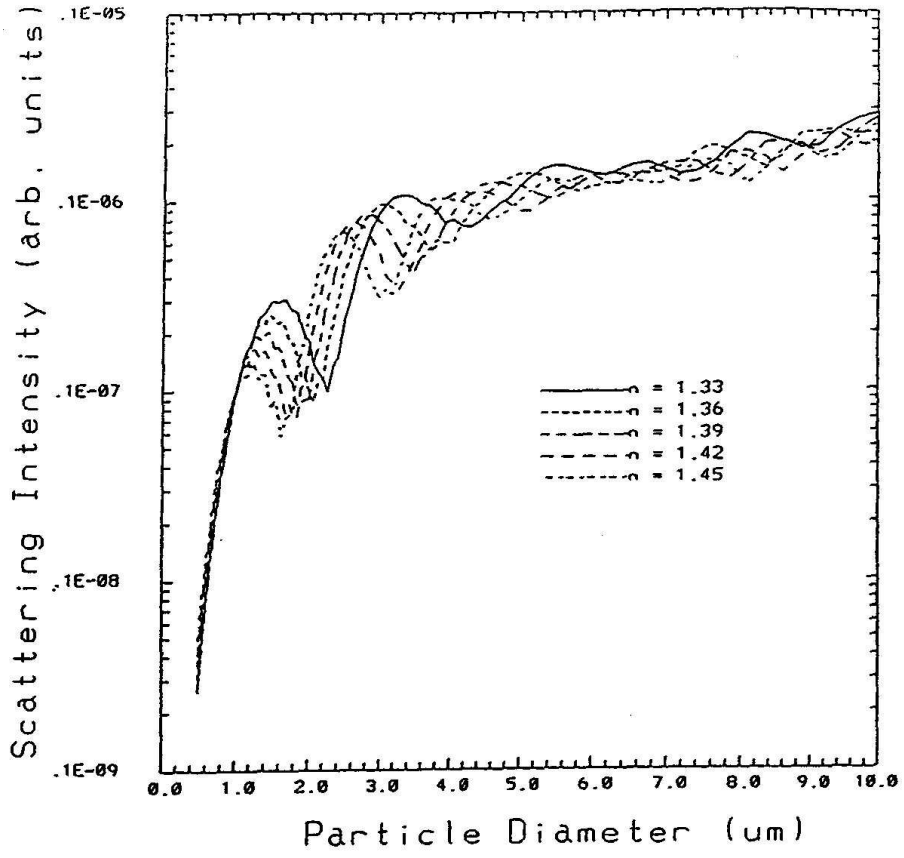


Figure 3.2: FSSP-300 theoretical Mie scattering curves for different indices of refraction, relating scattering intensity to particle size (from Baumgardner et al., 1992). Pure ice has a refractive index of of 1.31.

The CAS bins particles into 30 bins between 0.52 and 44.3 $\mu$m. Fig. 3.2 shows that especially between 1 and 5 $\mu$m diameter, converting scattering intensity to particle size can be ambiguous. Because this ambiguity appeared to cause an artificial spike in the concentration of ice crystals around 1 $\mu$m, five bins between 0.98 and 2.70 $\mu$m were combined. Furthermore, although small crystals are likely to be quasi-spherical (Spinhirne et al., 1998; Meyer et al., 2002), deviations from an assumed spherical shape can lead to biases in size calculations (Baumgardner et al., 1992). Baumgardner et al. (1992) estimate a total sizing uncertainty of about 30% based on combined uncertainties associated with Mie scattering ambiguities, ice crystal shape and variable laser beam intensity.

The optical extinction coefficient $\beta_{ext}$ was calculated using measurements from a Gerber Scientific, Inc. Cloud Integrating Nephelometer (CIN) (Gerber et al., 2000). The CIN integrates the phase function (Eq. 2.7) over all scattering angles between 10° and 175°to obtain $\beta_{ext}$. The fraction of light scattered outside of the angular domain of the CIN is estimated to be 0.57$\pm$0.02 (Gerber et al., 2000). A 635 nm laser beam light scattered by atmospheric particles is measured using four Lambertian sensors that act as photomultipliers (see Fig. 3.3). Due to excess light leakage and photomultiplier shot noise, the threshold detection is about 0.4 km$^{-1}$. The error for clouds twice as optically thick reduces to about 15%. The

sampling frequency of the CIN is 1 Hz and the sampling volume is 3 L per m $s^{-1}$ flight speed ($\sim 0.6$ $m^3$ $s^{-1}$ for this study).

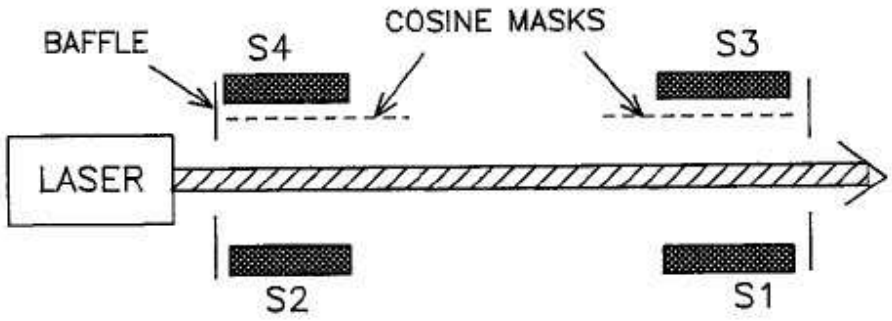


Figure 3.3: Schematic diagram (not to scale) representing a side view of the CIN instrument. A 635 nm laser beam is scattered by airborne particles into four Lambertian sensors (labeled S1 through S4) that consist of a light-diffusing disk and a photomultiplier. S1 and S3 measure forward scattered light, while S2 and S4 measure backscattered light. Both S3 and S4 measurements are weighted by the cosine of the scattering angle using a cosine mask (from Gerber et al., 2000).

The CIN instrument has uniform response to ice crystals between 4 $\mu$m and 2.5 mm diameter, but overestimates optical extinction from particles less than 4 $\mu$m diameter (Fig. 3.4). This is because small ice crystals have similar sizes to the wavelength of the laser and increase the percentage of light that is backscattered to the sensors. The fractional overestimate $F$ depends on $r_e$ according to the third-order equation (T. Garrett, pers. comm.):

$$F = -0.027r_e^3 + 0.30r_e^2 - 1.0r_e + 2.3. \tag{3.1}$$

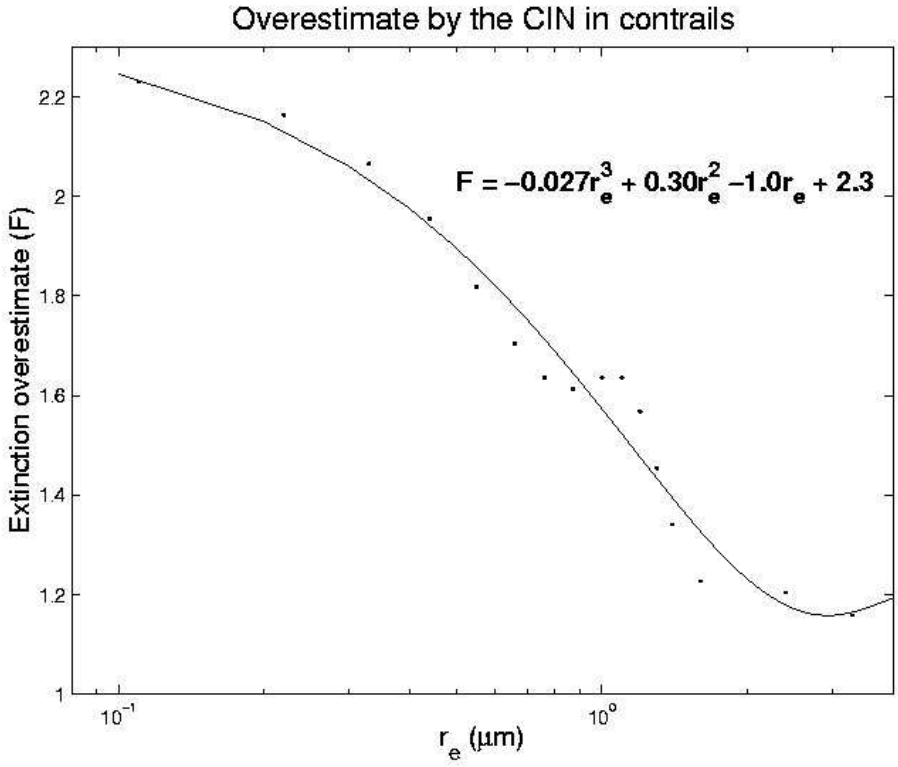


Figure 3.4: Plot of the overestimation of extinction by the CIN in contrails as a function of particle size, based on the size distribution for the 13 July contrail case and the corresponding equation of correction (from T. Garrett, pers. comm.).

The correct value of $\beta_{ext}$ in clouds where the diameter of the ice crystals is predominantly less than 4 $\mu$m is therefore $\beta_{ext}/F$. Because this is the case in the 13 July contrail event, future references to "$\beta_{ext}$" refer to the corrected value.

### 3.3 Meteorological and geographical measurements

Relative humidity data were obtained using the Jet Propulsion Labo-

ratory (JPL) near-infrared spectrometer. The spectrometer contains a tunable diode laser light source, operating at a wavelength of 1.37 $\mu$m, and an open-path multipass Herriott cell for high precision ($\pm$0.05 ppmv) $H_2O$ detection over a 2-s measurement integration period. The instrument is accurate to within $\pm$5 % (R. May, 1998).

The Meteorological Measurement System (MMS) instrument was used to measure ambient pressure, temperature, and wind fields, and the position, orientation and velocity of the aircraft. The instrument contains three major components: An air motion sensing system to measure the velocity of the air with respect to the aircraft (true air speed or TAS); a Litten LTN-72 inertial navigation system (INS) to measure the velocity of the aircraft with respect to the earth (ground speed); and a data acquisition system to sample, process and record the measured quantities at a sampling frequency of 1 Hz. The air motion system consists of sensors that measure temperature, pressure and airflow angles with respect to the aircraft (Scott et al., 1990).

Wind vectors were derived from a combination of the air motion system and INS data and calculations. The main sources of error are inaccuracies in attitude (pitch, roll and heading) measurements, which can cause erroneous TAS readings. Because the TAS is an order of magnitude larger than horizontal wind speed, small errors in TAS lead to relatively large

errors in wind fields. The precision of the instrument is 0.1 mb, 0.1 K, and 0.1 m $s^{-1}$ for pressure, temperature, and horizontal and vertical wind velocity measurements, respectively; the accuracy is $\pm$0.03 mb ($\sim$0.5 %), $\pm$0.3 K ($\sim$0.2 %), $\pm$ 1 m $s^{-1}$($\sim$3.3%) and $\sim$0 m $s^{-1}$ for pressure, temperature, horizontal wind, and vertical wind, respectively (Scott et al., 1990). Flight coordinates (latitude, longitude, and altitude) were also taken from the INS, which contains an imbedded Global Positioning System (GPS).

# CHAPTER 4

# CONTRAIL CASE OBSERVATIONS

On 13 July, 2002, the WB-57F produced a contrail as it flew westward over the southwest coast of Florida gradually descending from about 16 to 15 km altitude over a ∼20-minute period between 1908 to 1928 UTC covering a horizontal distance of ∼220 km. The aircraft then circled back (see Fig. 4.1) to sample its contrail between 1932 and 1952 UTC as it flew eastward along the plume's length.

Fig. 4.1 shows photographs looking westward of the WB-57 forming and sampling its contrail. Fig. 4.1 c) and d) show a new contrail forming within the initial contrail, which had spread horizontally between 1 and 1.5 km (see Sec. 4.4) in the intervening of ∼25 minutes.

## 4.1 Case meteorological conditions

Ambient temperature, humidity and wind shear determine a contrail's properties and evolution (Jensen et al., 1998; Kärcher, 2000; others). Fig. 4.2 shows an atmospheric sounding obtained as the WB-57F descended from the lower stratosphere (∼20 km) to the surface on its descent into

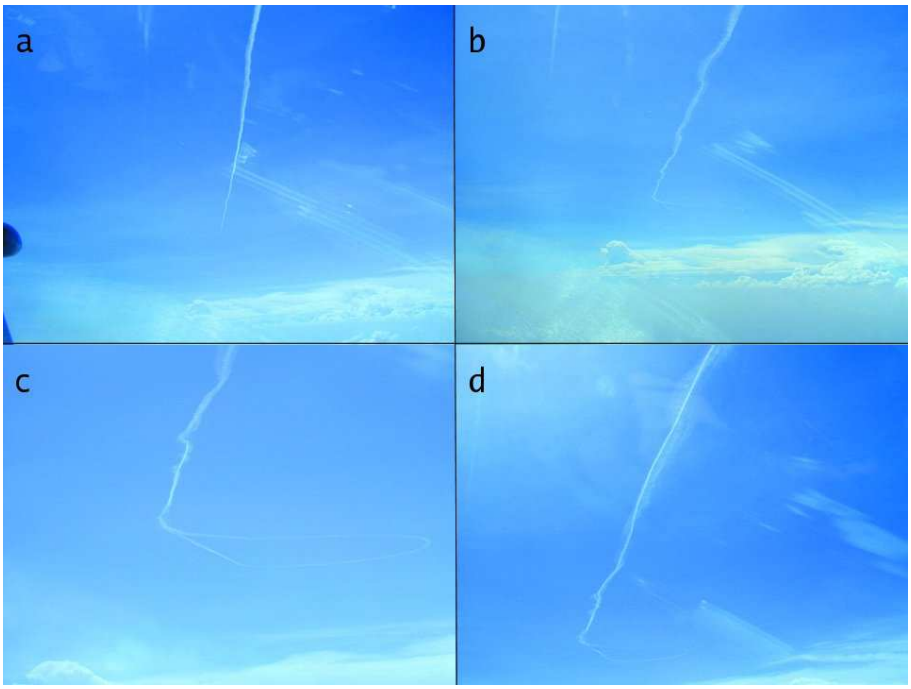


Figure 4.1: a) Generation of the WB-57F contrail; b) Initial WB-57F penetration (sampling) of its plume; c) Generation of a new contrail within the sampled plume; and d) Spreading of the original plume after ∼25 minutes. The photographs were taken from the Twin Otter aircraft as it flew beneath the contrail at about 1 km altitude. The photos were taken about 5 minutes apart.

Key West.

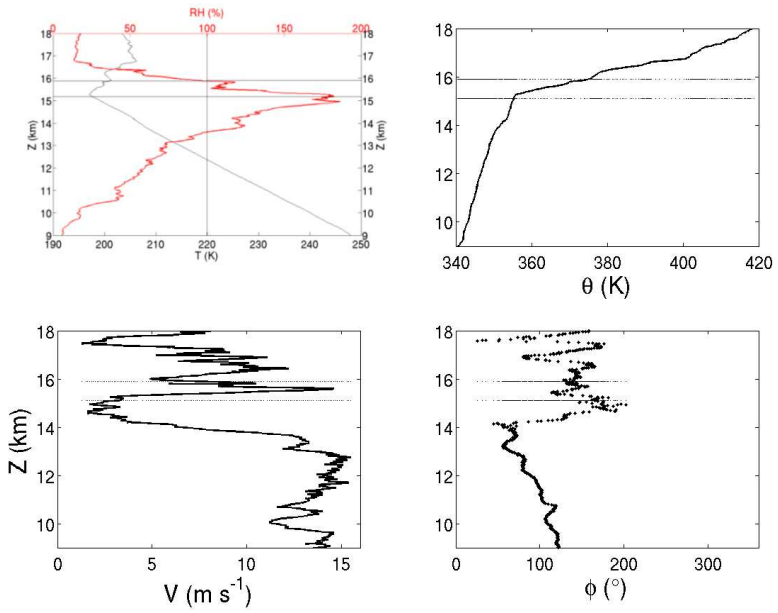


Figure 4.2: Vertical profile of the upper troposphere and lower stratosphere taken from the WB-57F during its initial descent into Key West: a) temperature and relative humidty (over ice), b) potential temperature $\theta$, c) horizontal wind speed $V$ and d) cardinal wind direction $\phi$. The horizontal lines at 15.1 and 15.9 km represent the bounds of contrail formation.

The sampled contrail formed between 15.1 km and 15.9 km altitude above a stable and cloud-free portion of the upper troposphere. The UT was particularly conducive to contrail formation and persistence due to high ambient values of $RH_i$, which ranged between $\sim$180% at 15.1 km and $\sim$100% at 15.9 km altitude.

The potential temperature gradient $d\theta/dz$ ranged from $\sim$2.5 K km$^{-1}$ in the UT to $\sim$25 K km$^{-1}$ above 15.4 km. Vertical wind shear $dV/dz$ was

about $2.0 \times 10^{-2}$ s$^{-1}$. The Richardson number $R_i$, defined as

$$R_i = \frac{\frac{g}{T}\frac{d\theta}{dz}}{(\frac{dV}{dz})^2}, \tag{4.1}$$

where $g$ is the gravitational constant 9.8 m s$^{-1}$ and $T$ is the temperature, was equal to about 10 at the altitude of the contrail, which suggests that high atmospheric stability had effectively supressed shear-generated turbulence within the contrail.

## 4.2 Contrail identification and age

The WB-57F sampled the length of its plume between 1932 and 1952 UTC. Because the WB-57F contrail formed in clear air, perturbations in the number density $N$ of small ice crystals $< 3$ $\mu$m indicate where the contrail plume was sampled. Ambient aerosol concentrations were generally < 0.1 cm$^{-3}$, while values of $N$ in the contrail were on the order of 100 cm$^{-3}$; hence $N$ and the perturbation $\Delta N$ are used interchangably here. Perturbations in CO, a by-product of fuel combustion, were calculated using as a baseline a spline curve fit through values in clear air. These are concurrent with perturbations in light extinction $\beta_{ext}$. Fig. 4.3 shows measurements of $N$, $\beta_{ext}$ and CO in the contrail as a function of contrail age.

Multiple penetrations of the contrail by the WB-57F resulted from the

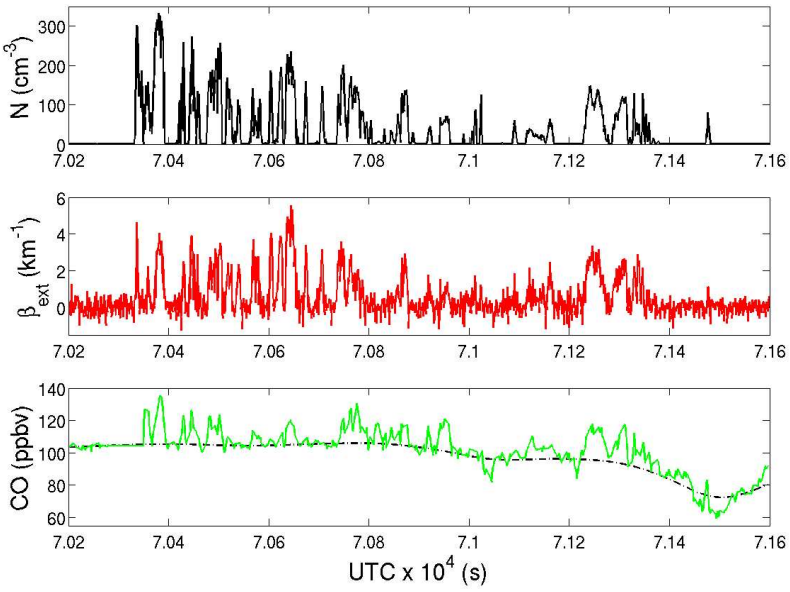


Figure 4.3: Plot of the ice crystal number density $N$, extinction coefficient $\beta_{ext}$ and CO concentration and their perturbations as the WB-57F flew through the length of its contrail on 13 July, 2002. The dashed line in the bottom plot represents values for CO using a spline curve through values in clear air.

plume “buckling” along its central axis (Fig. 4.1). The age of the contrail at each penetration was calculated by temporally and spatially aligning the contrail sampling leg of the flight with the corresponding contrail producing leg and using MMS wind and coordinate data. The age of the contrail at the first penetration (the time taken for the WB-57F to produce the elliptical contrail in Fig. 4.1) was 268 s with an estimated uncertainty of about 10 s. The greatest source of uncertainty is the high temporal and spatial variability of the horizontal wind that results in uncertainty in the magnitude and direction of contrail advection.

### 4.3 Ice crystal flux from the WB-57F

The WB-57F consumes JP-5 fuel, chemical composition $C_{10}H_{19}$, at a mean rate of 0.33 kg $s^{-1}$(B. Barnett, private comm.). The main combustion products are $CO_2$ and $H_2O$ (vapor) combined with trace quantities of $O_2$, O, CO, $H_2$ and H (Way et al., 1999). The balanced chemical equation for combustion of JP-5 is

$$4C_{10}H_{19} + 59O_2 \rightarrow 40CO_2 + 38H_2O. \tag{4.2}$$

The correlation between the measured concentrations of ice crystals $N_{ice}$ and CO shown in Fig. 4.3 is used here to estimate the total flux $J_{ice}$ of ice crystals from the WB-57F (per second). This flux estimate provides a means to estimate the contrail plume horizontal spreading and vertical

depth.

The flux $J_{ice}$ is estimated from the rate of fuel combustion and perturbations of $CO_2$ within the plume. Unfortunately, direct measurements of $CO_2$ were not taken on 13 July due to instrument failure; however, here we estimate $CO_2$ perturbations based on the measured perturbations in CO, assuming proportionality $F_1$ between $CO_2$ and CO in the combustion by-products. The value of $CO_2$ on 13 July is estimated from measurements of CO and $CO_2$ in a WB-57F contrail plume sampled on 23 July at an altitude of 13.8 km and a temperature and pressure of -65$^o$C and 162 mb, respectively. The value of $F_1$, the ratio of perturbations of $CO_2$ to CO, in the 23 July contrail was equal to about 35.

The value for $J_{ice}$ was calculated by:

$$J_{ice} = J_{JP5} F_M F_N, \tag{4.3}$$

where $J_{JP5}$ is the flux of JP-5, $F_M$ is the mass ratio of $CO_2$ to JP-5 as predicted by Eq. 4.2, and $F_N$ is the ratio of $\Delta N_{ice}$ to $\Delta CO_2$ (divided by the density of $CO_2$ in air). This calculation yielded a value for $J_{ice}$ of $7.6 \times 10^{14}$ s$^{-1}$. The corresponding number of ice crystals emitted per unit mass of fuel burned $J_m$ is $2.3 \times 10^{15}$ kg$^{-1}$. This value of $J_m$ is considerably higher than values of $J_m$ reported by Paladino et al. (1998) in a NASA B757 plume, by Gierens et al. (1996) using numerical simulations, and

by Jensen et al. (1998) also using numerical simulations (by one, two and three orders of magnitude, respectively). On the other hand, the above value of $J_m$ is similar (within a factor of two) to those found in many earlier studies of contrails from commercial aircraft such as the Boeing 737 (e.g., Anderson et al., 1998; Shröder et al., 2000; Spinhirne et al., 1998; Ström and Gierens, 2002).

The estimated uncertainty in measured values of $N_{ice}$ is about 25% (Baumgardner et al., 1992), but the uncertainty in $J_{ice}$ may be much higher, because these calculations assumed that all ice crystals in the contrail originated only from aerosols emitted by the WB-57F, and not from entrainment by ambient air (Jensen et al., 1998). Here we also assumed that all aerosols emitted by the WB-57F become activated as condensation nuclei. While Anderson et al. (1998) assumed that only one-third of all aerosols emitted from commercial aircraft between 9 and 12 km altitude became activated, the probability of nucleation becomes very high for the low temperatures and high supersaturations observed here (Kärcher, 2000).

## 4.4 Spatial properties and evolution

The vertical depth $\Delta z$ of the WB-57F contrail was not directly measured. However, assuming the contrail has a rectangular cross-section, $\Delta z$ can be estimated based on the plume's width $w$, the flux of ice crystal nuclei from the WB-57F $J_{ice}$, the ice crystal number density $N$ and the true

air speed of the aircraft $v$:

$$\Delta z = \frac{J_{ice}}{Nvw}, \tag{4.4}$$

where $J_{ice}$ and $v$ are $7.6 \times 10^{14}$ s$^{-1}$ and 191 m s$^{-1}$, respectively, and $N$ is the mean concentration of ice crystals measured in the contrail (see Fig. 4.4). We estimate the width of the contrail $w$ by calculating the diameter of the loop (assuming it is circular) shown in Fig. 4.1 based on the mean speed of the aircraft and the time taken to complete the full loop. From this calculated loop diameter ($\sim$16.6 km) and the ratio of the number of photograph pixels in the diameter to the width of the contrail, we infer an initial plume width of $\sim$200 m. The value of $w$ increased to about 1.5 km when the contrail was $\sim$30 minutes old.

From Eq. 4.4, the corresponding initial contrail depth $\Delta z$ is $\sim$150 m. Previous studies indicate that most contrails spread horizontally from a few hundred meters shortly after formation to a few km over a 30- to 60-minute period (Jensen et al., 1998; Khvorostyanov and Sassen, 1998; Sassen, 1997, Spinhirne et al., 1998). Meanwhile, $\Delta z$ is usually $\sim$100 m shortly after formation and increases to about 0.5 km after 30 to 60 minutes (Chlond, 1998; Jensen et al., 1998; Ponater et al., 2002; Sassen, 1997; Spinhirne et al., 1998). Therefore, the calculated initial plume dimensions are fairly consistent with earlier observations.

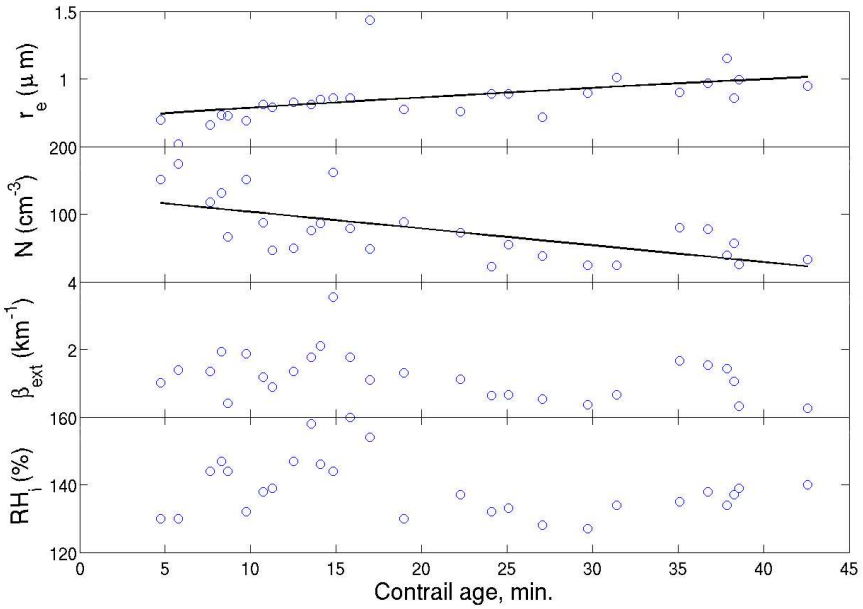


Figure 4.4: From top to bottom: Ice crystal effective radius $r_e$, number density $N_{ice}$, extinction $\beta_{ext}$, and the relative humidity over ice $RH_i$ are all plotted against contrail age in minutes.

This method for calculating $\Delta z$ assumes that the total number of ice crystals inside the plume is conserved, i.e., it does not account for nucleation of new ice crystals as the contrail evolves. The contrail width $w$ increased much more rapidly (by about a factor of 8 over 30 minutes) than $N$ decreased (from about 150 to 50 or by a factor of 3 over 30 minutes) (Fig. 4.4). Mathematically this may be interpreted as implying a nearly three-fold decrease in plume depth over time; however, previous observations of contrails indicate that this is unlikely: plumes spread. Rather, we hypothesize that the depth of the plume remained relatively constant, but that new ice crystals were being rapidly nucleated in ambient air entrained

into the contrail and forced upward by updrafts (Jensen et al., 1998). It is important to note that the rate of decrease in $N$ may be underestimated here; we assumed a linear decrease (Fig. 4.4). Some authors (e.g., Jensen et al., 1998; Kärcher, 2000) have estimated initial ice crystal concentrations as high as $10^5$ cm$^{-3}$, suggesting an exponential decrease.

Based on the respective uncertainties in $N$ and $w$ of 25% and 30%, the estimated uncertainty in the calculated initial $\Delta z$ is $\sim$40%. Additional uncertainty may be introduced from the assumption that the plume's cross section is rectangular: modeling studies have shown that contrail cross sections evolve into complex shapes more closely resembling figure-eights or ellipses for young contrails and triangles, trapezoids or "U" shapes for mature contrails more than a few minutes old (Chlond 1998; Jensen et al., 1998; Ström and Gierens, 2002).

## 4.5 Microphysical and bulk properties

This section presents and discusses measurements for the microphysical and bulk properties of the ice crystals as the contrail evolved. Fig. 4.4 shows all of these properties with respect to contrail age.

### 4.5.1 Ice crystal size

Fig. 4.5 shows size distributions of the WB-57F contrail ice crystals. The size distributions represent averages of the first and second halves of

the contrail penetrations shown in Fig. 4.4. The mean ages were ∼10 minutes and ∼30 minutes, respectively.

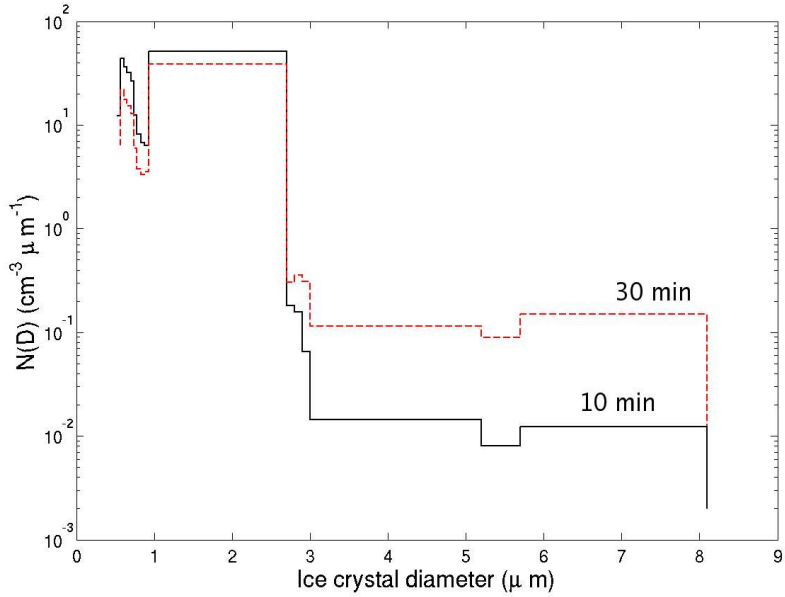


Figure 4.5: Size distribution of ice crystals inside the contrail when it was 10 minutes old (solid line) and 30 minutes old contrail (dashed line).

Contrail ice crystals were predominantly smaller than 3 $\mu$m diameter, but as the contrail aged, the concentrations of ice crystals larger than 3 $\mu$m increased, while the relative number of ice crystals smaller than 3 $\mu$m decreased. No ice crystals larger than 8 $\mu$m diameter were observed. The total initial concentration $N$ of ice crystals was ∼150 cm$^{-3}$ decreasing to ∼50 cm$^{-3}$ after 45 minutes. Although some authors (e.g., Baumgardner et al., 1998; Chlond, 1998; Heymsfield et al., 1998) report similar values of $N$ in contrails, the concentrations of ice crystals in the WB-57F contrail are an order of magnitude higher than those observed in most previous studies

(e.g., Goodman et al., 1998; Jensen et al., 1998; Khorostyanov and Sassen, 1998; Sassen, 1997; Twohy et al., 1998). Assuming total water inside the plume is conserved, the relatively high values of $N$ in the WB-57F contrail are consistent with the small ice crystal sizes that were measured.

Assuming the ice crystals were spherical, the mean effective radius $r_e$ calculated for each plume penetration was based on the measured size distributions. Values of $r_e$ increased slowly from 0.7 $\mu$m for young contrails less than 10 minutes old to about 1.0 $\mu$m for mature contrails greater than 30 minutes old. Observed values of $r_e$ were an order of magnitude smaller than those observed previously in contrails measured at lower altitudes (e.g., Jensen et al., 1998; Lawson et al., 1998; Marquart et al., 2003) (see Table 1.1).

Ice crystal growth rates were unusually slow considering the saturation ratio with respect to ice was $\sim$1.4 inside the plume. In a supersaturated environment, ice crystals grow according to Eq. 2.15. A least-squares fit to the $r_e$ data points (shown in Fig. 4.4) yields the equation

$$r_e(t) = \sqrt{(0.49 + 1.3 \times 10^{-2} t)}, \tag{4.5}$$

where $t$ is in minutes. However, according to Eq. 2.15, if the contrail ice crystals grew due to the observed saturation ratio, then

$$r_e(t) \approx \sqrt{\left((r_0)^2 + 0.1t\right)}. \tag{4.6}$$

The reason for the large discrepancy between theoretical and observed growth rates is not clear. Gao et al. (2003) have proposed that nitric acid trihydrate (NAT) can raise the equilibrium saturation ratio over ice to over 1.3. NAT or NAT-like molecules form at temperatures below 202 K when $HNO_3$ (nitric acid) combines with surface $H_2O$ molecules. The NAT inhibits uptake of atmospheric $H_2O$ onto ice surfaces more than it inhibits ice crystal sublimation. The observed saturations of $\sim$1.4 are only slightly above equilibrium saturation ratios proposed for NAT conditions and are therefore more consistent with observed gradual growth of the ice crystals.

### 4.5.2 Bulk properties

From Eq. 2.12, the ice water content $W$ is a function of the extinction coefficient $\beta_{ext}$ and effective radius $r_e$:

$$W = \frac{2}{3} r_e \rho \beta_{ext}. \tag{4.7}$$

Average values of $\beta_{ext}$ and $W$ inside the contrail were about $\sim$1.5 km$^{-1}$ and $\sim$0.7 mg m$^{-3}$, respectively. There was no obvious trend in either $\beta_{ext}$ or $W$ as the plume evolved. These magnitudes and trends are most similar to those from researchers (e.g., Khvorostyanov and Sassen, 1998; Twohy, 1998) who observed ice crystal sizes similar to those shown in this study.

Although Eq. 4.7 assumes $Q_{ext} = 2$, which may not have been the case here because the incident wavelength and ice crystal sizes were similar,

these estimates of $W$ appear to be fairly accurate. Mean values of $W$ from the Harvard Total Water instrument, which directly measured $W$ at 0.1 Hz within 5% accuracy, indicate $W = 0.9$ mg m$^{-3}$ in the contrail.

Optical depth $\tau$ is derived from the extinction measurements and vertical depth estimates (from Sec. 4.4) according to Eq. 2.6. Assuming the estimated vertical thickness of 0.15 km, the mean value of $\tau$ generally was $\sim$0.2, which is typical for contrails (e.g., Duda et al., 1998; Minnis et al., 1995; Ponater et al., 2002; Sassen, 1997). Some researchers (e.g., Spinhirne et al., 1998) have noted that $\tau$ decreases as the contrail ages. Although the newly formed contrail appeared to be optically thicker than the old (sampled) contrail, based on the digital images in 4.1, calculated values for $\tau$ show no obvious trend as the contrail evolved.

# CHAPTER 5

# RADIATIVE EFFECTS

## 5.1 The Streamer model

Here we use the radiative transfer model Streamer (Key, 2001) to examine the radiative impact of contrails located at the tropopause. The Streamer model uses a discrete ordinate solver to calculate radiative fluxes and radiances using two or more streams in both the infrared and shortwave spectra. For our calculations, four streams for shortwave and two streams for longwave fluxes are used. Streamer includes several built in surface reflectance schemes and single-scattering properties for various ice crystal habits. Here it is assumed that a rough aggregates scattering model (Yang and Liou, 1998) best represents contrail ice crystal scattering properties for shortwave calculations, while in the longwave spectra, ice crystals are approximated as spheres.

The primary motivation for the Streamer calculations is to examine the potential climate impact of moving flights to higher altitudes by comparing the radiative effects of contrails at the tropopause with the radiative effects of contrails at commercial cruise altitudes. Contrails at the tropopause

(15 km) are simulated by setting the single-scattering properties according to the in situ measurements in the WB-57F plume. Young (<5-minute old) and mature (>30-minute old) contrails at lower altitudes (10 km) are simulated using typical values observed in previous studies. Sensitivity experiments are performed to see how ice crystal size and water content affect the values of $CRF_{net}$.

Surface emissivity, land and ocean temperatures, vertical profiles and land coverage were defined according to Hartmann (1994). The chosen geographical location and atmospheric conditions (approximately) represent global mean conditions. Further details of the user-defined input variables and atmospheric conditions are outlined below in Tables 5.1 and 5.2.

Table 5.1: Streamer input variables

| Variable | Value |
|---|---|
| Date | March 20 |
| Mid-latitude | 45° N |
| Tropical latitude | 25° N |
| Global mean temperature | 10° C |
| Tropical mean temperature | 25° C |
| Surface emissivity | 94% |
| Ice crystal habit (shortwave) | rough aggregates |
| Ice crystal habit (longwave) | spheres |
| Contail top temperature (tropical latitude, tropopause) | -75° C |
| Contrail top temperature (mid-latitude, tropopause) | -70° C |
| Contrail top temperature (mid-latitude, 10 km) | -60° C |
| Plume thickness (mid-latitude young & tropopause contrails) | 150 m |
| Plume thickness (mid-latitude mature contrails) | 500 m |
| $r_e$ (mid-latitude tropopause contrails) | 1 $\mu$m |
| $r_e$ (mid-latitude young, 10 km contrails) | 5 $\mu$m |
| $r_e$ (mid-latitude mature, 10 km contrails) | 20$\mu$m |

Table 5.2: Land coverage

| Cover Type | Cover % |
|---|---|
| Ocean (global) | 70 |
| Green vegatation (tropical) | 30 |
| Bare sea ice | 3 |
| Dry sand | 8 |
| Green vegetation | 4 |
| Green grass | 7 |
| Dry grass | 4 |
| Coniferous forest | 4 |

## 5.2 Radiative forcing results

### 5.2.1 Comparison with lower altitude contrails

Fig. 5.1 shows the net radiative forcing $CRF_{net}$ at the TOA from contrails located at the tropopause (15 km) and young and mature contrails located at 10 km (plotted as a function of $WP$). The estimated values of $WP$ from the WB-57F (0.15 g m$^{-2}$) and typical aircraft (1.5 g m$^{-2}$) are drawn vertically on the plot to predict the value of $CRF_{net}$ associated with each type of aircraft.

For adequate comparison between contrails at the tropopause and contrails at 10 km, we make two important assumptions: one is that the value of $r_e$ is proportional to temperature as suggested in Fig. 1.1; the other is that the total amount of water inside the plume is conserved (Spinhirne et

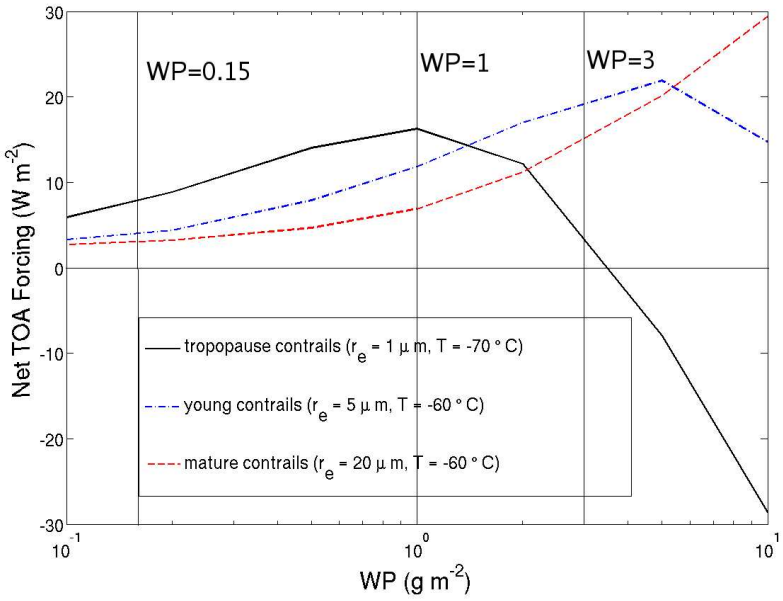


Figure 5.1: Diurnally averaged (with a time resolution of 1 hour) net (longwave plus shortwave) CRF at the TOA as a function of $WP$ for a) contrails at the tropopause ($z = 15$ km; $r_e = 1$ $\mu$m), b) young contrails at 10 km ($r_e = 5$ $\mu$m) and c) mature contrails at 10 km ($r_e = 20$ $\mu$m). All calculations assume a whole-sky, single-layer contrail coverage at 45° N latitude on the Vernal equinox and no clouds beneath or above the contrails. Ranges of typical ice water paths for small aircraft ($0.1$ g m$^{-2} \leq WP \leq 0.15$ g m$^{-2}$) and large aircraft (1 g m$^{-2} \leq WP \leq 3$ g m$^{-2}$) are indicated by the vertical lines superimposed on the plot (see references in Table 1.2).

al., 1998). Assuming conservation of total water mass, the value of $WP$ should be proportional to the water vapor flux from the aircraft, which, as shown in Eq. 4.2, is proportional to the fuel combustion rate. Therefore, $WP$ depends on the aircraft (and fuel) type. Fuel combustion rates have not been extensively studied; however, in contrails from aircraft that have similar ice nuclei fluxes to the WB-57F, the value of $WP$ should be similar if the combustion rate is similar.

While increasing the value of $WP$ generally increases the net forcing (Marquart et al., 2003), there is a "critical value" of $WP$ that maximizes the value of $CRF_{net}$. Increasing the value of $WP$ beyond this critical value decreases the net forcing, because the effects of solar reflection increase more rapidly than the effects of thermal regulation; eventually, the solar forcing becomes dominant and the sign of $CRF_{net}$ becomes negative. Fig. 5.1 shows that the critical value of $WP$ is about 1.0 g $m^{-2}$ for contrails at the tropopause; the tropopause contrail $CRF_{net}$ curve crosses the 10 km altitude young and mature contrail $CRF_{net}$ curves at about 1.3 and 2.0 g $m^{-2}$, respectively.

We therefore suggest that the climate forcing from contrails produced by small aircraft (which have small $H_2O$ fluxes yielding water paths less than about 2 g $m^{-2}$) would be minimized (decreased by roughly 50%) by flying at lower altitudes, while forcing from persistent contrails produced

by large aircraft with high $H_2O$ fluxes ($WP > 2$ g m$^{-2}$) would be minimized by moving flights up to the tropopause. This is because for $WP > 2$ g m$^{-2}$, the smaller effective radius of the high-altitude contrail increases the optical depth enough to cause shortwave forcing to dominate.

Finally, Fig. 5.1 shows that in warmer contrails (where $r_e$ changes significantly) the radiative properties evolve as the plume ages. The results are consistent with previous observations such as those by Marquart et al. (2003): as the contrail matures and ice crystals grow (hence $\tau$ decreases), $CRF_{net}$ decreases, except for contrails with $WP > 4$ g m$^{-2}$ where the opposite is true and $\tau$ and $CRF_{net}$ are inversely correlated. This further stresses the importance of accurately determining the value of $WP$, especially in contrails produced by larger aircraft.

### 5.2.2 Sensitivity of CRF to ice crystal size

A second study was conducted to determine the sensitivity of $CRF_{net}$ to ice crystal size. In this study, in situ data from the WB-57F contrail were used but for global mean conditions at tropical latitudes (25° N).

Fig. 5.2 shows that the value of $CRF_{net}$ is highly sensitive to ice crystal size. The differences in $r_e$ between contrails at the tropopause ($r_e = 1$ $\mu$m) and contrails at 10 km ($r_e = 5$ and 20 $\mu$m for young and mature contrails, respectively) would therefore explain most of the differences in the character of each curve in Fig. 5.1. For thin contrails ($WP = 0.1$

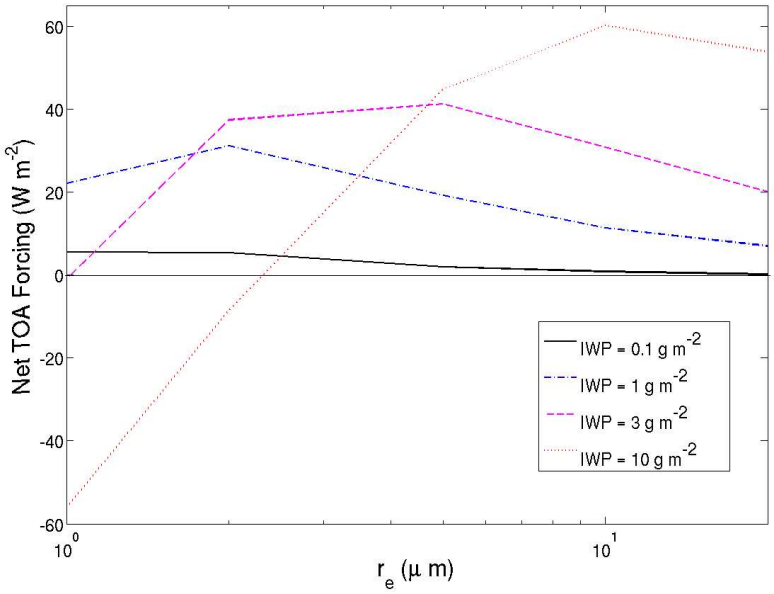


Figure 5.2: Net forcing at the TOA as a function of $r_e$ in contrails at the tropopause (at 15 km altitude and -75$^o$ C) for $WP = 0.1$ g m$^{-2}$, $WP = 1$ g m$^{-2}$, $WP = 3$ g m$^{-2}$, $WP = 10$ g m$^{-2}$ at a latitude of 25$^o$ N.

g m$^{-2}$), $CRF_{net}$ is inversely correlated with $r_e$. This is because small ice crystals more effectively absorb and emit infrared radiation (Garrett et al., 2003), thereby increasing their IR effect, while still allowing high penetration of solar radiation. For thicker contrails however ($WP \geq 1.0$ g m$^{-2}$), the correlation between $r_e$ and $CRF_{net}$ is positive for small ice crystals and becomes negative beyond a "critical" value of $r_e$ that depends on the value of $WP$.

We therefore conclude that the differences in the radiative properties between contrails at the tropopause and contrails at 10 km are primarily because values of $r_e$ are small at cold temperatures and do not increase

significantly with contrail age.

# CHAPTER 6

# DISCUSSION AND CONCLUSIONS

## 6.1 Summary of results

This thesis has presented in situ data and observations from a contrail produced by the NASA WB-57F in the tropopause between 15 and 16 km on 13 July, 2002 during CRYSTAL-FACE. The contrail formed at a temperature of -75° C and pressure of 125 mb in the absence of clouds and in a stable and highly supersaturated layer of the UT. The WB-57F penetrated its own plume multiple times during a 20-minute period between 1932 and 1952 UTC. Photographs of the contrail from the Twin Otter showed the plume spreading to an estimated width of 1 to 1.5 km over a $\sim$25-minute period.

Based on ratios of perturbations in $N$, CO and $CO_2$ within the contrail the ice crystal flux per unit mass of JP-5 fuel burned was determined to be $2.3 \times 10^{15}$ kg$^{-1}$. Assuming the plume cross-section was rectangular, based on an estimated plume width of 200 m the contrail depth was 150$\pm$60 m. Because the plume spread horizontally by a greater factor than $N$ decreased, and assuming that the plume's vertical thickness remained

nearly constant, new ice crystals were continually being generated inside the plume during entrainment of ambient air.

The WB-57F contrail was characterized by unusually high concentrations of small ice crystals. Initial concentrations were $\sim$150 cm$^{-3}$ dropping to $\sim$50 cm$^{-3}$ after $\sim$45 minutes. The effective radius $r_e$ of the ice crystals increased from about 0.7 to 1.0 $\mu$m over the same 45-minute period and averaged 0.8 $\mu$m inside the plume. These values of $r_e$ were on average about an order of magnitude smaller than those observed at lower altitudes (10 km) and were most similar to values seen in studies at higher altitudes (13 km) (e.g., Goodman et al., 1998; Jensen et al., 1998, Khorostyanov and Sassen, 1998; Liou et al., 1998). These observations were consistent with the hypothesized correlation between ice crystal size and temperature discussed in Chapter 1.

It has been argued that at extremely cold temperatures below 202 K ice crystals became coated with nitric acid trihydrate (NAT), which raises the equilibrium saturation ratio to about 1.3 (Gao et al., 2003). This might explain the observed slow growth of the ice crystals despite the high values of saturation ratio of about 1.4 measured inside the plume.

Ice water content $W$ inside the plume averaged 0.7 mg m$^{-3}$ with an estimated ice water path $WP$ of 0.1 g m$^{-2}$. The optical extinction coefficient averaged 1.5 km$^{-1}$, which corresponds to $\tau = 0.2$, assuming a

vertical plume thickness of 150 m.

## 6.2 Climate implications

Model simulations of the WB-57F contrail, using the in situ measurements from 13 July, 2002, and contrails at lower altitudes show that moving aircraft flight to higher altitudes would increase the contrail's net radiative forcing $CRF_{net}$ at the top of the atmosphere by about 5 to 10 W m$^{-2}$ for low values (less than 2 g m$^{-2}$) of $WP$, e.g., for small aircraft that do not produce large quantities of $H_2O$. On the other hand, moving flight to higher altitudes would minimize the $CRF_{net}$ at the TOA if the value of $WP$ is greater than 2 g m$^{-2}$, e.g., for large commercial aircraft with high $H_2O$ fluxes. The differences in the values of $CRF_{net}$ between the tropopause and lower altitude contrails increase to several 10s of W m$^{-2}$for $WP > 3$ g m$^{-2}$, where the sign of the forcing by the tropopause contrail becomes negative due to the dominance of shortwave forcing.

Sensitivity studies show that the decrease in $r_e$ with $T$ can account for most of the differences between the forcing by the tropopause contrail and mid-altitude contrails. While $r_e$ appears to be primarily a function of temperature, the $WP$ is most probably a function of the type and size of the aircraft producing the contrail.

Climate modeling studies require a consideration of the frequency of contrail formation. Fig. 2.2 shows that contrails would be more likely

to form at higher altitudes, particularly over low latitudes. This would of course increase the sky coverage of contrails, as would the projected increase in air traffic by Meyer et al. (2002). Also, an estimated 10 to 20 percent of all cirrus, which covers about 20 to 30 percent of the earth's surface and accounts for one third to half of all cloud cover, is thought to originate from contrails (Khvorostyanov and Sassen, 1998; Schröder et al., 2000), which means that as much as 2 to 6 percent of the sky (globally averaged) is probably covered by contrail-induced cirrus. Sassen (1997), Minnis et al. (2004) and others have noted significant increases in cirrus cover in regions of heavy flight traffic. Therefore, not only contrails, but contrail-induced cirrus, should be considered in climate models.

The effects of coexisting natural cloud cover were not considered in this study. Clouds, which cover about 60 percent of the earth (Hartmann, 1994), would reduce the longwave component of the forcing more substantially than the shortwave and would decrease the net forcing by nearly one order of magnitude (Ponater et al., 2002).

The balance between contrail radiative effects and greenhouse forcing from aircraft $CO_2$ emission is unclear. While this research suggests that large aircraft flying at cold temperatures may emit enough $H_2O$ to change the sign of the contrail radiative forcing, large aircraft also emit greater quantities of $CO_2$, which persists substantially longer in the atmosphere

than do contrails. The total annual emission of $CO_2$ depends on fuel type, combustion rate and efficiency and the total annual flight time integrated over all flights, and is not easily estimated.

The WB-57F contrail presented here represents the first time a contrail was studied in detail at the tropopause. An area of future improvement would be to complement the in situ measurements with remote sensing observations, since this would assist determination of the spatial structure and evolution of the plume aside from the photographs from the Twin Otter. For example, lidar observations of the plume would have filled this void and decreased the uncertainty in the optical depth calculations, therefore improving radiative transfer calculations.

Finally, more measurements of contrails at or near the tropopause need to be conducted to adequately understand the relationship between temperature and ice crystal size. If contrail ice crystals from large aircraft at high altitudes can be shown to be sufficiently small to significantly reduce the value or change the sign of the net radiative forcing, then by encouraging flight at cold temperatures, it may be possible to mitigate the climate impact of $CO_2$ emissions from jet aircraft.

## REFERENCES


Anderson, B. E., W. R. Cofer, D. R. Bagwell, J. W. Barrick, C. H. Hudgins, 1998: Airborne observations of aircraft aerosol emissions I: Total nonvolatile particle emission indeces. *Geophys. Res. Lett.,* **25**, 1689-1692.

Bailey, M. and J. Hallett, 2004: Growth rates and habits of ice crystals between -20$^{o}$C and -70$^{o}$C. *J. Atmos. Sci.*, **61**, 514-544.

Baumgardner, D., J. E. Dye, B. W. Gandrud, and R. G. Knollenberg, 1992: Interpretation of measurements made by the forward scattering spectrometer probe (FSSP-300) during the airborne arctic stratospheric expedition. *J. Geophys. Res.*, **97**, 8035-8046.

Baumgardner, D., and B. E. Gandrud, 1998: A comparison of the microphysical and optical properties of particles in an aircraft contrail and mountain wave cloud. *Geophys. Res. Lett.,* **25**, 1129-1132.

Chlond, A., 1998: Large-eddy simulation of contrails. *J. Atmos. Sci.*, **55**, 796-819.

Coleman, R. F., 1996: A new formulation for the critical temperature of contrail formation. *J. Applied Met.*, **35**, 2270-2284.

Duda, D. P., J. D. Spinhirne, and W. D. Hart, 1998: Retrieval of contrail microphysical properties during SUCCESS by the split window method. *Geophys. Res. Lett.*, **25**, 1149-1152.

Duda, D. P., P. Minnis, L. Nguyen, and R. Palikonda, 2004: A case study of the development of contrail clusters over the great lakes. *J. Atmos. Sci.,* **61**, 1132-1146.

Gao, R. S., P. J. Popp, D. W. Fahey, T. P. Marcy, R. L. Herman, E. M. Weinstock, D. G. Baumgardner, T. J. Garrett, K. H. Rosenlof, T. L. Thompson, P. T. Bui, B. A. Ridley, S. C. Wofsy, O. B. Toon, M. A. Tolbert, B. Kärcher, Th. Peter, P. K. Hudson, A. J. Weinheimer, and A. J. Heymsfield, 2003: Evidence that ambient nitric acid increases relative humidity in low-temperature cirrus clouds. *Science*, **303**, 516-520.

Garrett, T. J., H. Gerber, D. G. Baumgardner, C. H. Twhoy, E. M. Weinstock, 2003: Small, highly reflective ice crystals in low-latitude cirrus. *Geophys. Res. Lett.*, **30**, 2132-2135.

Gayet, J.-F., G. Febvre, G. Brogniez, H. Chepfer, W. Renger, and P. Wendling, 1996: Microphysical and physical properties of cirrus and contrails: Cloud field study on 13 Octover 1989. *J. Atmos. Sci.*, **53**, 126-138.

Gerber, H., Y. Takano, T. J. Garrett, and P. V. Hobbs, 2000: Nephelometer measurements of the asymmetry parameter, volume extinction coefficient, and backscatter ratio in Arctic clouds. *J. Atmos. Sci.*, **57**, 3021-3034.

Gierens, K. M., 1996: Numerical Simulations of Persistent Contrails. *J. Atmos. Sci.*, **53**, 3333-3348.

Goodman, J., R. F. Pueschel, E. J. Jensen, S. Verma, G. V. Ferry, S. D. Howard, S. A. Kinne, and D. Baumgardner, 1998: Size and shape of contrails ice particles. *Geophys. Res. Lett.*, **25**, 1127-1130.

Hagen, P., D. Whitefield, J. Paladino, and M. Trueblood, 1998: Particle sizing and emission indeces for a jet engine exhaust sampled at cruise. *Geophys. Res. Lett.*, **25**, 1681-1684.

Hartmann, D. L., 1994: Global physical climatology. Academic Press, 411 pp.

Heymsfield, A. J., R. P. Lawson, and G. W. Sachse, 1998: Growth of ice crystals in a precipitation contrail. *Geophys. Res. Lett.*, **25**, 1335-1338.

Jensen, E. J., A. S. Ackerman, D. E. Stevens, O. B. Toon, and P. Minnis, 1998: Spreading and growth of contrails in a sheared environment. *J. Geophys. Res.*, **103**, 31557-31567.

Jensen, E. J., O. B. Toon, R. F. Pueschel, J. Goodman, G. W. Sasche, B. E. Anderson, K. R. Chan, D. Baumgardner, and R. C. Miake-Lye, 1998: Ice crystal nucleation and growth in contrails forming at low ambient temperatures. *Geophys. Res. Lett.*, **25**, 1371-1374.

Kärcher, B., 2000: Contrails: Observations, formation mechanisms, atmospheric impacts, uncertainties. Contrib. to *Identifying the uncertainties in radiative forcing in climate aviation contrails and aviation-induced cirrus*, UK Defense Evaluation and Research, 41 pp.

Kärcher, B., and Lohmann, 2002: A parameterization of cirrus cloud formation: homogeneous freezing including effects of aerosol size. *J. Geophys. Res.*, **107**, 4698-4707.

Key, J. R., 2001: Streamer user's guide. Cooperative Institute for Meteorological Satellite Studies, The University of Wisconsin, 96 pp.

Khvorostyanov, V., and K. Sassen, 1998: Cloud model simulation of a contrail case study: Surface cooling against upper tropospheric warming. *Geophys. Res. Lett.*, **25**, 2145-2148.

Lawson, R. P., A. J. Heymsfield, S. M. Aulenbach, and T. L. Jensen, 1998: Sizes, shapes and light scattering properties of ice crystals in cirrus and contrails during SUCCESS. *Geophys. Res. Lett.*, **25**, 1331-1334.

Lewellen, D. C., and W. S. Lewellen, 2001: The effects of aircraft wake dynamics on contrail development. *J. Atmos. Sci.*, **58**, 390-406.

Liou, K. N., 2002: An introduction to atmospheric radiation. 2d ed. Academic Press, 583 pp.

Liou, K. N., P. Yang, Y. Tahano, K. Sassen, T. Charlock, and W. Arnott, 1998: On the radiative properties of contrail cirrus. *Geophys. Res. Lett.*, **25**, 1161-1164.

Marquart, S., M. Ponater, F. Mager and R. Sausen, 2003: Future development of contrail cover, optical depth, and radiative forcing: Impacts of increasing air traffic and climate change. *J. Climate*, **16**, 2890-2904.

May, R. D., 1998: Open-path, near-infrared tunable diode laser spectrometer for atmospheric measurements of $H_2O$. *J. Geophys. Res.*, **103**, 19161-19172.

Meyer R. H. Mannstein, R. Meerkötter, U. Schumann, and P. Wendling, 2002: Regional radiative forcing by line-shaped contrails derived from satellite data. *J. Geophys. Res.*, **107**, 17-1 to 17-15.

Minnis, P., D. P. Kratz, J. A. Coakley, III, M. D. King, D. Garber, P. Heck, S. Mayor, D. F. Young, and R. Arduini, 1995: Cloud optical property retrieval (Subsystem 4.3). Clouds and the Earth's Radiant Energy System (CERES) Algorithm Theoretical Basis Document: Cloud Analyses and Improved Top of Atmosphere Fluxes. *NASA RP 1376*, **3**,135-176.

Minnis, P., J. K. Ayers, M. L. Nordeen, and S. P. Weaver, 2003: Contrail frequency over the United States from surface observations. *J. Climate*, **16**, 3447-3462.

Minnis, P., J. K., Ayers, R. Palikonda, and D. Phan, 2004: Contrails, cirrus trends and climate. *J. Climate.*, **17**, 1671-1685.

Paladino, J., P. Whitefield, D. Hagen, A. R. Hopkins, M. Trueblood, 1998: Particle concentration characterization for jet engine emissions under cruise conditions. *Geophys. Res. Lett.*, **25**, 1697-1700.

Ponater, M., S. Marquart, and R. Sausen, 2002: Contrails in a comprehensive global climate model: Parameterization and radiative forcing results. *J. Geophys. Res.*, **107**, 2-1 to 2-18.

Pruppacher, H. R. and J. D. Klett, 1997: Microphysics of clouds and precipitation. 2d ed. Kluwer Academic Publishers, 954 pp.

Reist, P. C., 1993: Aerosol Science and Technology. 2d ed. (insert publisher)

Rogers, R. R. and M. K. Yau, 1989: A short course in cloud physics. 3d ed. Butterworth Heinemann, 290 pp.

Sassen, K., 1997: Contrail-cirrus and their potential for regional climate change. *Bull. Amer. Meteor. Soc.*, **78**, 1885-1903.

Sassen, K., and C. Hsueh, 1998: Contrail properties derived from high-resolution polarization lidar studies during SUCCESS. *Geophys. Res. Lett.*, **25**, 1165-1168.

Schröder, F., B. Kärcher, C. Duroure, J. Strom, A. Petzold, J.-F. Gayet, B. Strauss, P. Wendling, and S. Borrmann, 2000: On the transition of contrails into cirrus clouds. *J. Atmos. Sci.*, **57**, 464-480.

Scott, S. G., T. P. Bui, K. R. Chan, and S. W. Bowen, 1990: The meteorological measurement system on the NASA ER-2 aircraft. *J. Atmos. Ocean. Tech.*, **7**, 525-540.

Spinhirne, J. D., W.D. Hart, and D. P. Duda, 1998: Evolution of morphology and microphysics of contrail cirrus from airborne remote sensing. *Geophys. Res. Lett.*, **25**, 1153-1156.

Stephens, G. L., G. W. Paltridge and C. M. R. Platt, 1978: Radiation profiles in extended water clouds III: Observations. *J. Atmos. Sci.*, **35**, 2133-2141.

Ström, L., K. Gierens, 2002: First simulations of cryoplane contrails. *J. Atmos. Ocean. Tech.*, **107**, 4346-4358.

Toon, O. B., and R. C. Miake-Lye, 1998: Subsonic Aircraft: Contrail and Cloud Effects Special Study (SUCCESS). *Geophys. Res. Lett.*, **25**, 1109-1112.

Travis, D. J., A. M. Carleton, and S. A. Changnon, 1997: An empirical model to predict widespread occurrences of contrails. *J. Applied Met.*, **36**, 1211-1220.

Travis, D. J., A. M. Carleton, and R. G. Lauritsen, 2004: Regional variations in U.S. diurnal temperature range for the 11-14 September 2001

aircraft groundings: Evidence of jet contrail influence on climate. *J. Climate*, **17**, 1123-1134.

Twohy, C. H., and B. W. Gandrud, 1998: Electron microscope analysis of residual particles from aircraft contrails. *Geophys. Res. Lett.*, **25**, 1359-1362.

Way, D. and J. Olds, 1999: SCORES: Web-based rocket propulsion analysis for space transportation system design. Contrib. to 35th AIAA/ASME/SAE/ASEE Joint Propulsion Conference and Exhibit, 20-24 June 1999, Los Angelos, CA.

Wyser, K., and J. Ström, 1998: A possible change in cloud radiative forcing due to aircraft exhaust. *Geophys. Res. Lett.*, **25**, 1673-1676.

Yang, P., and K. N. Liou, 1998: Single scattering properties of complex ice crystals in terrestrial atmosphere. *Contr. Atmos. Phys.*, **71**, 223-248.

Young, D. F., P. Minnis, D. Baumgardner, H. Gerber, 1998: Comparison of in situ and satellite-derived properties during SUCCESS. *Geophys. Res. Lett.*, **25**, 1125-1128.

Flight track data was obtained from the website: http://angler.larc.nasa.gov/crystal/fltdays/wb57_071302_new/

All other data used for this study was obtained from the CRYSTAL-FACE website: http://cloud1.arc.nasa.gov/crystalface/